

Enhancing Low-resolution Image Representation Through Normalizing Flows*

Chenglong Bao[†] Tongyao Pang[‡] Zuowei Shen[§] Dihan Zheng[¶] Yihang Zou^{||}

Abstract

Low-resolution image representation is a special form of sparse representation that retains only low-frequency information while discarding high-frequency components. This property reduces storage and transmission costs and benefits various image processing tasks. However, a key challenge is to preserve essential visual content while maintaining the ability to accurately reconstruct the original images. This work proposes LR2Flow, a nonlinear framework that learns low-resolution image representations by integrating wavelet tight frame blocks with normalizing flows. We conduct a reconstruction error analysis of the proposed network, which demonstrates the necessity of designing invertible neural networks in the wavelet tight frame domain. Experimental results on various tasks, including image rescaling, compression, and denoising, demonstrate the effectiveness of the learned representations and the robustness of the proposed framework.

Key words. low-resolution representation, normalizing flow, wavelet tight frame, multi-scale representation, reconstruction error analysis

1 Introduction

With the rapid advancement of imaging devices, both the volume and resolution of acquired images have increased significantly, posing substantial challenges for transmission and storage. While applying standard compression techniques or reducing resolution via downsampling are natural approaches, they raise a fundamental question: *How can one obtain a low-resolution (LR) image that allows for the accurate reconstruction of its high-resolution (HR) counterpart?* This challenge is known as the *LR representation* problem. Mathematically, let $\mathbf{x} \in \mathbb{R}^n$ denote an HR image, and let its LR representation reside in \mathbb{R}^d with $d < n$. Our objective is to design a downscaling operator $\varphi : \mathbb{R}^n \rightarrow \mathbb{R}^d$ and an upscaling operator $\psi : \mathbb{R}^d \rightarrow \mathbb{R}^n$ that satisfy

$$\mathbf{x} \approx \psi(\varphi(\mathbf{x})) \quad \text{and} \quad \varphi(\mathbf{x}) \approx \downarrow_{n/d}(\mathbf{k}^{\text{lp}} * \mathbf{x}), \quad (1)$$

where \mathbf{k}^{lp} , $*$, and $\downarrow_{n/d}$ denote a predefined low-pass filter, the convolution operator, and the downsampling operator with a rate of n/d , respectively. We refer to $\varphi(\mathbf{x})$ as the LR representation of \mathbf{x} . The first condition in (1) ensures the reconstructibility of the HR image, while the second encourages the preservation of global appearance. Consequently, this model yields a compact surrogate representation well-suited for compression and edge-to-cloud collaborative inference in low-bandwidth scenarios [13, 51, 41]. The resulting framework

*Submitted to the editors DATE. This work was partially supported by National Key R&D Program of China (No.2021YFA1001300), the National Natural Science Foundation of China (No.12271291), the New Cornerstone Investigator Program (NCI202310).

[†]Yau Mathematical Sciences Center, Tsinghua University, Beijing, China, and Beijing Institute of Mathematical Sciences and Applications, Beijing, China (clbao@tsinghua.edu.cn)

[‡]Yau Mathematical Sciences Center, Tsinghua University, Beijing, China (typang@tsinghua.edu.cn).

[§]Department of Mathematics, National University of Singapore, Singapore (matzuows@nus.edu.sg).

[¶]Department of Pharmaceutical Chemistry, University of California, San Francisco, CA, USA (dihan.zheng@ucsf.edu).

^{||}Yau Mathematical Sciences Center and Department of Mathematical Sciences, Tsinghua University, Beijing, China (zouyh21@mails.tsinghua.edu.cn).

is applicable to a wide range of tasks, including image rescaling [51, 30, 6, 48], image compression [6, 53, 50], and image restoration [32].

LR representation is closely related to sparse representation. In the classical setting, one seeks a sparse coefficient vector $\mathbf{c} \in \mathbb{R}^N$ for an image $\mathbf{x} \in \mathbb{R}^n$ such that $\mathbf{W}^\top \mathbf{c} \approx \mathbf{x}$, where \mathbf{W} is a predefined wavelet tight frame [38, 17] or a data-driven transformation [2, 37, 10]. One typical construction of \mathbf{W} involves selecting a low-pass filter \mathbf{k}^{lp} and a set of high-pass filters $\{\mathbf{k}_i^{\text{hp}}\}_{i=1}^r$ that satisfy certain extension principles. We define $\mathbf{W} = (\mathbf{W}_L^\top, \mathbf{W}_H^\top)^\top$, where the low- and high-frequency decomposition operators are given by

$$\mathbf{W}_L : \mathbf{x} \mapsto \downarrow_2 (\mathbf{k}^{\text{lp}} * \mathbf{x}) \in \mathbb{R}^{\frac{n}{2}}, \quad \mathbf{W}_H : \mathbf{x} \mapsto (\downarrow_2 (\mathbf{k}_1^{\text{hp}} * \mathbf{x}); \dots; \downarrow_2 (\mathbf{k}_r^{\text{hp}} * \mathbf{x})) \in \mathbb{R}^{\frac{nr}{2}}$$

The sparse coefficient \mathbf{c} is typically formed by preserving the low-frequency coefficient $\mathbf{x}_L = \mathbf{W}_L \mathbf{x}$ and applying a nonlinear thresholding operator (or a variant) [20] to the high-frequency coefficients $\mathbf{x}_H = \mathbf{W}_H \mathbf{x}$. This results in the representation $\mathbf{c} = (\mathbf{x}_L, \mathcal{T}(\mathbf{x}_H))$, where \mathcal{T} denotes the thresholding-induced nonlinear mapping. Thus, \mathbf{c} becomes an LR representation when $\mathcal{T}(\mathbf{x}_H) = \mathbf{0}$. In this setting, $d = n/2$, the downscaling and upscaling operators are

$$\varphi : \mathbf{x} \mapsto [\mathbf{W} \mathbf{x}]_{1:d}, \quad \psi : \mathbf{y} \mapsto \mathbf{W}^\top (\mathbf{y}; \mathbf{0}_{N-d}),$$

where $\mathbf{u}_{s:t} = (u_i)_{s \leq i \leq t}$ denotes sub-vectors, and $\mathbf{0}_{N-d} \in \mathbb{R}^{N-d}$ is a zero vector. While the downscaling operator $\varphi(\mathbf{x})$ preserves the primary visual features of \mathbf{x} , the reconstructed image $\psi(\varphi(\mathbf{x})) = \mathbf{W}_L^\top \mathbf{W}_L \mathbf{x}$ inevitably suffers from a loss of high-frequency information.

Motivated by the above observations, we propose a framework that jointly learns the downscaling and upscaling operators within a designed *invertible* architecture, with the goal of enhancing the recovery of high-frequency information. Specifically, let $\mathbf{W} \in \mathbb{R}^{N \times n}$ be a wavelet tight frame and let $\mathcal{F} : \mathbb{R}^N \rightarrow \mathbb{R}^N$ denote an invertible mapping. The downscaling and upscaling operators φ and ψ are defined as

$$\varphi : \mathbf{x} \mapsto [\mathcal{F}(\mathbf{W} \mathbf{x})]_{1:d}, \quad \psi : \mathbf{y} \mapsto \mathbf{W}^\top \mathcal{F}^{-1} \circ \mathcal{E}(\mathbf{y}),$$

where $\mathcal{E} : \mathbb{R}^d \rightarrow \mathbb{R}^N$ is an extension operator. By construction, this design yields a compact latent representation. To further enhance reconstruction, we map the remaining coordinates $[\mathcal{F}(\mathbf{W} \mathbf{x})]_{(d+1):N}$ to a prior distribution p . This allows us to discard these components during transmission and restore them via sampling, effectively defining $\mathcal{E}(\mathbf{y}) = (\mathbf{y}, \mathbf{z})$ where $\mathbf{z} \sim p$. Consequently, the final downscaling and upscaling operators are formulated as

$$\varphi(\mathbf{x}) = [\mathcal{F}(\mathbf{W} \mathbf{x})]_{1:d}, \quad \psi(\mathbf{y}) = \mathbb{E}_{p(\mathbf{z})} [\mathbf{W}^\top \mathcal{F}^{-1}(\mathbf{y}, \mathbf{z})]. \quad (2)$$

We parameterize \mathcal{F} using invertible neural networks, such as Normalizing Flows (NFs) [18, 28] or Invertible Residual Networks (iResNets) [7], and apply this architecture progressively to the wavelet tight frame coefficients at each level. From a theoretical perspective, we analyze the reconstruction error of $\hat{\mathbf{x}} = \psi(\varphi(\mathbf{x}))$ obtained from the learned mapping, which provides insight into the necessity of designing a nonlinear \mathcal{F} to align with the underlying data distribution in order to obtain an effective LR representation. Furthermore, our derived reconstruction error bound demonstrates the theoretical advantage of using a redundant wavelet tight frame system over an orthonormal basis, which is also verified empirically through numerical experiments. Finally, we evaluate our model across various image processing tasks, demonstrating its superior performance and broad applicability.

Notations. We denote vectors using bold lowercase letters (e.g., \mathbf{a}), where a_i refers to the i -th component. Matrices are denoted by bold uppercase letters (e.g., \mathbf{A}), with A_{ij} representing the entry in the i -th row and j -th column. For a vector $\mathbf{u} \in \mathbb{R}^m$ and integers $1 \leq s \leq t \leq m$, we define the slice $\mathbf{u}_{s:t} = (u_i)_{s \leq i \leq t}$. The ℓ_p -norm of a vector \mathbf{u} is defined as $\|\mathbf{u}\|_p = (\sum_i |u_i|^p)^{1/p}$. Unless otherwise specified, $\|\mathbf{u}\|$ denotes the Euclidean norm $\|\mathbf{u}\|_2$.

2 Related Work

In this section, we briefly review related work on LR representation in the context of image rescaling and compression.

Image rescaling seeks a forward mapping from HR domain to LR representation and an inverse mapping for reconstruction. The goal is to produce visually coherent LR images that allow for faithful HR restoration. Prior works generally fall into three categories: (i) methods that fix the downscaling kernel (typically Bicubic interpolation) and train a super-resolution (SR) network for upscaling [19, 3, 31, 61, 15, 29, 12]; (ii) frameworks that jointly optimize downscaling and upscaling in an end-to-end encoder-decoder architecture [48, 27, 44]; and (iii) approaches employing NFs to model these stages as mutually invertible processes [51, 30, 6, 50]. However, categories (i) and (ii) often exhibit limited synergy between stages. By coupling downscaling and upscaling primarily through reconstruction loss, these methods lack geometric regularization and fail to exploit the reciprocal structure of the task or account for information loss inherent in downscaling [51]. In contrast, flow-based methods formulate rescaling as a multiscale bijection, enabling both visually consistent LR representations and robust reconstruction.

Although image rescaling inherently compresses data by reducing spatial resolution, applying standard lossy compression (e.g., JPEG) to the LR representation allows for significantly higher compression ratios. Consequently, this approach has emerged as a prominent research direction. Recent works [52, 53, 6] implement this strategy by employing a differentiable JPEG simulator to facilitate end-to-end training of the rescaling-based compression network. Furthermore, to mitigate distribution shifts induced by lossy compression in the LR domain, [53, 6, 50] utilize auxiliary JPEG decoders to eliminate compression artifacts.

While flow-based architectures have achieved significant success in image rescaling and compression, existing designs predominantly rely on a fixed orthogonal basis for frequency decomposition [32, 51, 50, 30, 6, 53]. Despite their empirical efficacy, a rigorous theoretical analysis of the reconstruction error in these methods remains largely unexplored. Furthermore, it is well-established that redundant representations enhance stability in image reconstruction [21, 14, 11, 24], as the corresponding inverse transformation operator possesses a nontrivial kernel. Motivated by this, we integrate invertible neural networks with wavelet tight frames to capitalize on these advantages. To the best of our knowledge, we present the first theoretical reconstruction error analysis for such an architecture.

3 The LR2Flow Model

This section presents the architecture of the proposed LR representation model, referred to as LR2Flow. Subsequently, we provide the approximation analysis of this model.

3.1 The Construction of LR2Flow

Recall from (2) that the downscaling and upscaling operators are $\varphi(\mathbf{x}) = [\mathcal{F}(\mathbf{W}\mathbf{x})]_{1:d}$ and $\psi(\mathbf{y}) = \mathbb{E}_{p(\mathbf{z})}[\mathbf{W}^\top \mathcal{F}^{-1}(\mathbf{y}, \mathbf{z})]$. In this work, we assume that \mathbf{z} is a random variable drawn from a standard Gaussian distribution. The operator $\mathbf{W} = (\mathbf{W}_L^\top, \mathbf{W}_H^\top)^\top$ is chosen as a wavelet tight frame generated by linear B-splines [9], which consists of one low-pass filter and two high-pass filters. Consequently, this transformation decomposes an input image $\mathbf{x} \in \mathbb{R}^n$ into a low-frequency coefficient vector $\mathbf{x}_L = \mathbf{W}_L \mathbf{x} \in \mathbb{R}^{n/2}$ and a high-frequency coefficient vector $\mathbf{x}_H = \mathbf{W}_H \mathbf{x} \in \mathbb{R}^n$. Assuming the LR representation dimension is $d = n/2^T$ for some integer T , we represent \mathcal{F} as the composition $\mathcal{F} = \mathcal{F}^{(T)} \circ \mathcal{F}^{(T-1)} \circ \dots \circ \mathcal{F}^{(1)}$, where

$$\mathcal{F}^{(l)} = \begin{cases} f^{(1)} : \mathbb{R}^{\frac{3n}{2}} \rightarrow \mathbb{R}^{\frac{3n}{2}}, & l = 1; \\ (f^{(l)} \circ \mathbf{W}) \times \text{Id}_{h_{l-1}} : \mathbb{R}^{\frac{n}{2^{l-1}}} \times \mathbb{R}^{h_{l-1}} \rightarrow \mathbb{R}^{\frac{3n}{2^l}} \times \mathbb{R}^{h_{l-1}}, & 2 \leq l \leq T. \end{cases}$$

Here, $h_l = 2n(1 - 2^{-l})$ denotes the total dimension of the high-frequency components accumulated from the previous l levels, $\text{Id}_{h_l} : \mathbb{R}^{h_l} \rightarrow \mathbb{R}^{h_l}$ represents the identity mapping, and $f^{(l)} : \mathbb{R}^{\frac{3n}{2^l}} \rightarrow \mathbb{R}^{\frac{3n}{2^l}}$ constitutes the flow at the l -th level. Specifically, $f^{(l)}$ comprises a sequence of M flow blocks, denoted as $f^{(l)} = f_M^{(l)} \circ \dots \circ f_1^{(l)}$. Each block $f_i^{(l)}$ consists of an ActNorm layer, an invertible 1×1 convolution [28], and a nonlinear invertible transformation $g_i^{(l)}$:

$$f_i^{(l)} = g_i^{(l)} \circ \text{Inv}_{1 \times 1} \circ \text{ActNorm}.$$

To define these components, let the input be $\mathbf{c}^{(l)} = (\mathbf{c}_0^{(l)}, \dots, \mathbf{c}_r^{(l)}) \in \mathbb{R}^{m_l}$, where $m_l = \frac{3n}{2^l}$ is the total dimension of the wavelet coefficients at level l . Recall that $r = 2$ represents the number of high-pass filters; each sub-vector $\mathbf{c}_k^{(l)}$ lies in $\mathbb{R}^{\frac{m_l}{r+1}}$. Here, $\mathbf{c}_0^{(l)}$ corresponds to the low-frequency component, while $\mathbf{c}_k^{(l)}$ corresponds to the k -th high-frequency subband for $1 \leq k \leq r$. The ActNorm transformation, parameterized by a scale vector $\mathbf{s} = (s_0, \dots, s_r) \in \mathbb{R}_{>0}^{r+1}$ and a bias vector $\mathbf{b} = (b_0, \dots, b_r) \in \mathbb{R}^{r+1}$, is defined as

$$\text{ActNorm}(\mathbf{c}^{(l)}; \mathbf{s}, \mathbf{b}) = (s_0 \mathbf{1}_{\frac{m_l}{r+1}} \odot \mathbf{c}_0^{(l)} + b_0 \mathbf{1}_{\frac{m_l}{r+1}}, \dots, s_r \mathbf{1}_{\frac{m_l}{r+1}} \odot \mathbf{c}_r^{(l)} + b_r \mathbf{1}_{\frac{m_l}{r+1}}), \quad (3)$$

where $\mathbf{1}_{m_l/(r+1)} \in \mathbb{R}^{\frac{m_l}{r+1}}$ is a vector of ones and \odot denotes the Hadamard product. The invertible 1×1 convolution, parameterized by an orthogonal matrix $\mathbf{K} \in \mathbb{R}^{(r+1) \times (r+1)}$, is expressed as

$$\text{Inv}_{1 \times 1}(\mathbf{c}^{(l)}; \mathbf{K}) = (\mathbf{K} \otimes \mathbf{I}_{m_l/(r+1)}) \mathbf{c}^{(l)}, \quad (4)$$

where $\mathbf{I}_{m_l/(r+1)} \in \mathbb{R}^{\frac{m_l}{r+1} \times \frac{m_l}{r+1}}$ denotes the identity matrix and \otimes denotes the Kronecker product. Finally, the nonlinear invertible transformation $g_i^{(l)}$ typically adopts one of two designs:

(i) An affine coupling layer [18]. This layer partitions the input $\mathbf{c}^{(l)}$ into a low-frequency part $\mathbf{c}_L^{(l)} = \mathbf{c}_0^{(l)}$ and a high-frequency part $\mathbf{c}_H^{(l)} = (\mathbf{c}_1^{(l)}, \dots, \mathbf{c}_r^{(l)})$, defined as

$$g_i^{(l)}(\mathbf{c}_L^{(l)}, \mathbf{c}_H^{(l)}) = (\mathbf{c}_L^{(l)}, \mathbf{c}_H^{(l)} \odot \exp(\rho_i^{(l)}(\mathbf{c}_L^{(l)})) + \eta_i^{(l)}(\mathbf{c}_L^{(l)})), \quad (5)$$

where $\rho_i^{(l)}, \eta_i^{(l)} : \mathbb{R}^{\frac{m_l}{r+1}} \rightarrow \mathbb{R}^{(1-\frac{1}{r+1})m_l}$ are parameterized neural networks.

(ii) An invertible residual block (iResBlock) [7]. This block is defined as

$$g_i^{(l)}(\mathbf{c}^{(l)}) = \mathbf{c}^{(l)} + \phi_i^{(l)}(\mathbf{c}^{(l)}), \quad \phi_i^{(l)} : \mathbb{R}^{m_l} \rightarrow \mathbb{R}^{m_l}, \quad \text{Lip}(\phi_i^{(l)}) \leq L < 1. \quad (6)$$

Since ActNorm, Inv $_{1 \times 1}$, and $g_i^{(l)}$ are invertible, each flow $f^{(l)}$ is guaranteed to be invertible. Combined with the perfect reconstruction property of \mathbf{W} , i.e., $\mathbf{W}^\top \mathbf{W} = \mathbf{I}$, the constructed \mathcal{F} constitutes a strictly invertible transformation with the inverse $\mathcal{F}^{-1} = (\mathcal{F}^{(1)})^{-1} \circ \dots \circ (\mathcal{F}^{(L)})^{-1}$, where each $(\mathcal{F}^{(l)})^{-1}$ is given by

$$(\mathcal{F}^{(l)})^{-1} = \begin{cases} (f^{(1)})^{-1} : \mathbb{R}^{\frac{3n}{2}} \rightarrow \mathbb{R}^{\frac{3n}{2}}, & l = 1; \\ (\mathbf{W}^\top \circ (f^{(l)})^{-1}) \times \text{Id}_{h_{l-1}} : \mathbb{R}^{\frac{3n}{2^{l-1}}} \times \mathbb{R}^{h_{l-1}} \rightarrow \mathbb{R}^{\frac{n}{2^{l-1}}} \times \mathbb{R}^{h_{l-1}}, & l \geq 2. \end{cases} \quad (7)$$

We now detail the computation of the downscaling and upscaling operators within the LR2Flow framework. The downscaling process proceeds hierarchically. Let $\mathbf{x}^{(0)} = \mathbf{x} \in \mathbb{R}^n$ denote the input image. During the forward pass at the l -th level, the input $\mathbf{x}^{(l-1)} \in \mathbb{R}^{\frac{n}{2^{l-1}}}$ is first decomposed via the wavelet tight frame into coefficients $(\mathbf{x}_L^{(l-1)}, \mathbf{x}_H^{(l-1)}) = \mathbf{W} \mathbf{x}^{(l-1)} \in \mathbb{R}^{\frac{n}{2^l}} \times \mathbb{R}^{\frac{2n}{2^l}}$. Subsequently, the flow network computes $(\mathbf{x}^{(l)}, \mathbf{z}^{(l)}) = f^{(l)}(\mathbf{x}_L^{(l-1)}, \mathbf{x}_H^{(l-1)})$. This operation fuses informative high-frequency details into the low-frequency subband to yield a refined representation $\mathbf{x}^{(l)} \in \mathbb{R}^{\frac{n}{2^l}}$, while simultaneously encoding residual information into the latent variable $\mathbf{z}^{(l)} \in \mathbb{R}^{\frac{n}{2^{l-1}}}$. Consequently, the forward transformation at the l -th level is expressed as

$$(\mathbf{x}^{(l)}, \mathbf{z}^{(l)}) = f^{(l)}(\mathbf{W} \mathbf{x}^{(l-1)}). \quad (8)$$

Based on this notation, the downscaling operator for \mathbf{x} is written as

$$\varphi(\mathbf{x}) = \mathbf{x}^{(T)}, \quad \text{where } \mathbf{x}^{(0)} = \mathbf{x}, \quad \mathbf{x}^{(l)} = [f^{(l)}(\mathbf{W} \mathbf{x}^{(l-1)})]_{1:n/2^l}, \quad l = 1, \dots, T.$$

Correspondingly, the upscaling operator is formulated as

$$\psi(\mathbf{y}) = \hat{\mathbf{x}}^{(0)}, \quad \text{where } \hat{\mathbf{x}}^{(T)} = \mathbf{y}, \quad \hat{\mathbf{x}}^{(l-1)} = \mathbb{E}_{p(\mathbf{z}^{(l)})} [\mathbf{W}^\top (f^{(l)})^{-1}(\hat{\mathbf{x}}^{(l)}, \mathbf{z}^{(l)})], \quad l = T, \dots, 1.$$

3.2 Reconstruction Error Analysis

Let $q(\mathbf{x})$ denote the distribution of the original HR images, with covariance $\Sigma = \text{Cov}[\mathbf{x}]$, and let the latent prior be given by $p = \mathcal{N}(\mathbf{0}, \sigma^2 \mathbf{I})$ with a temperature parameter $\sigma \geq 0$. This section presents a theoretical analysis of the reconstruction error by deriving an upper bound for the following quantity:

$$\mathbf{e}^* = \inf_{\mathcal{F} \in \Theta} \{ \mathbb{E}_{q(\mathbf{x})p(\mathbf{z})} \| \mathbf{x} - \mathbf{W}^\top \mathcal{F}^{-1}([\mathcal{F}(\mathbf{W}\mathbf{x})]_{1:d}, \mathbf{z}) \|^2 \}, \quad (9)$$

where $\mathbf{W} = (\mathbf{W}_L^\top, \mathbf{W}_H^\top)^\top$ satisfies $\mathbf{W}^\top \mathbf{W} = \mathbf{I}$, Θ denotes the hypothesis space of invertible neural networks. The quantity \mathbf{e}^* characterizes the reconstruction capability of different architectural choices. In the subsequent analysis, we focus on two representative classes of invertible architectures: the affine coupling layers defined in (5) and the invertible residual blocks described in (6).

Case I: affine coupling layers. As defined in (5), we consider a one-layer affine coupling structure. Then, the corresponding hypothesis space is given by

$$\Theta = \{ \mathcal{F} : (\mathbf{x}_L, \mathbf{x}_H) \mapsto (\mathbf{x}_L, \rho(\mathbf{x}_L) \odot \mathbf{x}_H + \eta(\mathbf{x}_L)) \mid \rho, \eta : \mathbb{R}^d \rightarrow \mathbb{R}^{N-d} \}. \quad (10)$$

The following proposition characterizes the optimal reconstruction error \mathbf{e}^* , defined in (9).

Proposition 1. *Let Θ be defined as in (10). Then, the minimal reconstruction error, defined in (9), satisfies*

$$\mathbf{e}^* = \mathbb{E}_{q(\mathbf{x})} \text{Tr} (\text{Var} [\mathbf{W}_H \mathbf{x} | \mathbf{W}_L \mathbf{x}] \mathbf{W}_H \mathbf{W}_H^\top). \quad (11)$$

The optimal solution ρ^ and η^* from the hypothesis space (10) satisfies: $\eta^*(\mathbf{x}_L) = -\rho^*(\mathbf{x}_L) \odot \mathbb{E}[\mathbf{W}_H \mathbf{x} | \mathbf{W}_L \mathbf{x} = \mathbf{x}_L]$.*

The proof of Proposition 1 is given in Appendix A. It is worth noting that the optimal value in (11) is equivalent to $\mathbb{E}_{q(\mathbf{x})} \|\mathbf{x} - \mathbb{E}[\mathbf{x} | \mathbf{W}_L \mathbf{x}] \|^2$. This implies that *an appropriately selected wavelet system can effectively capture the principal components of the data distribution within its low-frequency subband*.

Next, we extend the above result to a broader family of invertible maps:

$$\Theta := \{ \mathcal{F} : (\mathbf{x}_L, \mathbf{x}_H) \mapsto (\mathbf{x}_L, h(\mathbf{x}_H; \mathbf{x}_L)) \mid h(\cdot; \mathbf{x}_L) \text{ is invertible on } \mathbb{R}^{N-d} \}. \quad (12)$$

If Θ is given by (12), we show an upper bound of (9).

Proposition 2. *Let Θ be defined as in (12). The minimal reconstruction error, defined in (9), has the following form:*

$$\mathbf{e}^* \leq \text{Tr} ((\mathbf{W}_H^\top \mathbf{W}_H)^2 (\mathbf{I} - \mathbf{W}_L^\dagger \mathbf{W}_L) \Sigma (\mathbf{I} - \mathbf{W}_L^\dagger \mathbf{W}_L)), \quad (13)$$

where \mathbf{W}_L^\dagger is the Moore-Penrose inverse of \mathbf{W}_L .

We defer the proof of Proposition 2 to Appendix A.

Remark 1. *For a symmetric matrix \mathbf{A} , let $\lambda_i^\downarrow(\mathbf{A})$ and $\lambda_i^\uparrow(\mathbf{A})$ denote the i -th largest and i -th smallest eigenvalues of \mathbf{A} , respectively, and let $\mathbf{V}_i^\downarrow(\mathbf{A})$ denote the eigenspace associated with $\lambda_i^\downarrow(\mathbf{A})$. Let $J(\mathbf{W})$ denote the upper bound in (13). Then, we have*

$$\inf_{\mathbf{W}} \{ J(\mathbf{W}) \mid \mathbf{W}^\top \mathbf{W} = \mathbf{I} \} = \sum_{i=1}^{n-d} (\lambda_i^\uparrow(\mathbf{W}_H^\top \mathbf{W}_H))^2 \lambda_{i+d}^\downarrow(\Sigma). \quad (14)$$

Moreover, this minimum is attained when the low-frequency subspace aligns with the principal eigenspaces of the data covariance, i.e., $\text{Im}(\mathbf{W}_L^\top) = \bigoplus_{i=1}^d \mathbf{V}_i^\downarrow(\Sigma)$. Refer to Appendix A for the proof of (14). This characterization provides a criterion for constructing \mathbf{W} based on the eigendecomposition of the data covariance $\Sigma = \text{Cov}[\mathbf{x}]$, although accurately estimating Σ in practice may be challenging.

Case II: invertible residual blocks (iResBlocks). We consider the one-layer iResBlock architecture defined in (6), with the hypothesis space specified by

$$\Theta = \{\mathcal{F} : \mathbf{c} \mapsto \mathbf{c} + \phi(\mathbf{c}) \mid \phi : \mathbb{R}^N \rightarrow \mathbb{R}^N, \text{Lip}(\phi) \leq L < 1\}. \quad (15)$$

The following proposition establishes an upper bound on the optimal reconstruction error \mathbf{e}^* defined in (9).

Proposition 3. *Let Θ be defined as in (15). Then, the minimal reconstruction error defined in (9) satisfies the following bound:*

$$\mathbf{e}^* \leq \frac{\inf_{f \in \mathcal{K}} \sqrt{\mathbb{E}_{q(\mathbf{x})} \|(\mathbf{1}_d + f(\mathbf{W}_L \mathbf{x}))^2\|^2}}{(1-L)^2} \cdot \sqrt{\mathbb{E}_{q(\mathbf{x})} \text{Var}[\mathbf{W}_H \mathbf{x} | \mathbf{W}_L \mathbf{x}]_F^2}, \quad (16)$$

where $\mathbf{1}_d \in \mathbb{R}^d$ denotes the vector of all ones, and $\mathcal{K} = \{f : \mathbb{R}^d \rightarrow \mathbb{R}^d \mid \text{Lip}(f) \leq L\}$.

We detail the proof in Appendix B. Our analysis reveals that the upper bound of the optimal reconstruction error in (9) for the iResBlock architecture is primarily governed by the term $\mathbb{E}_{q(\mathbf{x})} \|\text{Var}[\mathbf{W}_H \mathbf{x} | \mathbf{W}_L \mathbf{x}]\|_F$. Consequently, designing an effective wavelet system for iResBlock architectures necessitates minimizing the conditional variance of the high-frequency subband. This requirement implies that *the low-frequency subband must retain the principal components of the data distribution*, a conclusion that aligns with our findings for the affine coupling layer.

Additionally, we analyze the case where $\Theta = O(N) = \{\mathbf{F} \in \mathbb{R}^{N \times N} \mid \mathbf{F}\mathbf{F}^\top = \mathbf{F}^\top\mathbf{F} = \mathbf{I}\}$. This analysis, detailed in Appendix C, highlights the inherent limitations of linear invertible mappings.

4 Applications of LR2Flow

In this section, we introduce the applications of LR2Flow in three image processing tasks.

Image rescaling

Image rescaling comprises two fundamental processes: downscaling a HR image to a LR version to reduce storage and transmission costs, and upscaling the LR image to restore the original resolution. The primary objective is to preserve visual appearance and detail fidelity while adjusting the resolution. This goal aligns closely with the task of learning effective LR representations, making LR2Flow a suitable framework. During downscaling, we generate the LR representation \mathbf{y} from the HR image \mathbf{x} via $\mathbf{y} = \varphi(\mathbf{x})$. Conversely, upscaling yields the HR reconstruction $\hat{\mathbf{x}}$ via $\hat{\mathbf{x}} = \psi(\mathbf{y})$. Inspired by [51, 50, 30], our training objective incorporates three components: (i) an HR reconstruction loss $\mathcal{L}_{\text{HR}} = \|\hat{\mathbf{x}} - \mathbf{x}\|_1$ that ensures fidelity between the reconstructed and original HR images; (ii) an LR guidance loss $\mathcal{L}_{\text{LR}} = \|\mathbf{y} - \text{Bic}(\mathbf{x})\|_2^2$ that aligns \mathbf{y} with a Bicubic-downsampled reference to maintain visual consistency, where $\text{Bic} : \mathbb{R}^n \rightarrow \mathbb{R}^d$ denotes the Bicubic interpolation operator; and (iii) a distribution matching loss $\mathcal{L}_{\text{dist}} = \|\mathbf{z}\|_2^2$ that aligns the model-induced latent distribution $([\mathcal{F} \circ \mathbf{W}]_{(d+1):N})_{\#} [q]$ with the prior $p = \mathcal{N}(\mathbf{0}, \sigma^2 \mathbf{I})$ by minimizing their cross-entropy. Here, $\mathbf{z} = [\mathcal{F}(\mathbf{W}\mathbf{x})]_{(d+1):N}$ denotes the high-frequency latent variable. The overall training objective for image rescaling is defined as

$$\mathcal{L} = \lambda_{\text{HR}} \mathcal{L}_{\text{HR}} + \lambda_{\text{LR}} \mathcal{L}_{\text{LR}} + \lambda_{\text{dist}} \mathcal{L}_{\text{dist}}, \quad (17)$$

where λ_{HR} , λ_{LR} , and λ_{dist} are hyperparameters.

Image compression

While image rescaling inherently conserves storage by reducing spatial resolution, applying standard lossy compression (e.g., JPEG) to the resulting LR image enables significantly higher compression rates. In this context, image compression can still be modeled as learning an LR representation, where the goal is to reconstruct the original image \mathbf{x} from the compressed representation $\mathbf{y} = \text{JPEG}(\varphi(\mathbf{x}))$, despite the

severe loss of high-frequency details. The training objective for compression task follows the formulation in (17). However, since the standard JPEG operator is non-differentiable, we employ a differentiable JPEG simulator [43, 52] during training to facilitate gradient backpropagation.

Image denoising

We extend LR2Flow to image denoising by interpreting the framework as a *refined frequency-domain decomposition method*: $(\mathbf{y}, \mathbf{z}) = (\mathcal{F} \circ \mathbf{W})(\mathbf{x})$. Here, \mathbf{y} denotes the refined low-frequency component and \mathbf{z} the high-frequency residual, with synthesis given by $\mathbf{W}^\top \circ \mathcal{F}^{-1}$. Leveraging the observation that *clean and noisy image pairs exhibit strong consistency in the low-frequency subband* [39, 22], we optimize LR2Flow to align the LR representations of the clean image \mathbf{x}_c and the noisy image $\mathbf{x}_n = \mathbf{x}_c + \mathbf{n}$. Formally, given the decompositions $(\mathbf{y}_c, \mathbf{z}_c) = (\mathcal{F} \circ \mathbf{W})(\mathbf{x}_c)$ and $(\mathbf{y}_n, \mathbf{z}_n) = (\mathcal{F} \circ \mathbf{W})(\mathbf{x}_n)$, our training objective is to ensure that $\mathbf{y}_c \approx \mathbf{y}_n$.

A naive denoising strategy involves modeling \mathbf{z}_c using a prior p and simply replacing \mathbf{z}_n with a sample from p during inference. However, disregarding the specific values of \mathbf{z}_n ignores the structural information it contains, frequently leading to over-smoothed results. To address this, we recover high-frequency details via $\hat{\mathbf{z}} = \mathcal{R}(\mathbf{z}_n; \mathbf{y}_n)$, employing a restoration network $\mathcal{R} : \mathbb{R}^{N-d} \times \mathbb{R}^d \rightarrow \mathbb{R}^{N-d}$. The final denoised image is then synthesized as $\hat{\mathbf{x}} = (\mathbf{W}^\top \circ \mathcal{F}^{-1})(\mathbf{y}_n, \hat{\mathbf{z}})$.

The training objective comprises three terms: (i) the image reconstruction loss $\mathcal{L}_{\text{img}} = \|\hat{\mathbf{x}} - \mathbf{x}_c\|_1$, which ensures fidelity; (ii) the low-frequency alignment loss $\mathcal{L}_{\text{lf}} = \|\mathbf{y}_n - \mathbf{y}_c\|_2^2$, designed to enforce consistency in the LR representations; and (iii) the high-frequency restoration loss $\mathcal{L}_{\text{hf}} = \|\mathbf{z}_c - \hat{\mathbf{z}}\|_2^2$. The total loss is defined as

$$\mathcal{L}_{\text{denoising}} = \lambda_{\text{img}} \mathcal{L}_{\text{img}} + \lambda_{\text{lf}} \mathcal{L}_{\text{lf}} + \lambda_{\text{hf}} \mathcal{L}_{\text{hf}}, \quad (18)$$

where λ_{img} , λ_{lf} , and λ_{hf} are weighting parameters.

5 Experiments

We evaluate LR2Flow on image rescaling, image compression, and image denoising tasks to demonstrate its effectiveness and versatility. All experiments are conducted on a single NVIDIA H800 GPU. Regarding the architectural configuration, we set the hierarchy level to $T = 1$ for the compression and denoising tasks. For image rescaling, we define $T = \log_2 s$, where s denotes the rescaling factor. Across all configurations, each flow level $f^{(l)}$ comprises $M = 8$ flow blocks, utilizing affine coupling layers to implement the invertible transformation $g_i^{(l)}$. In the reported results, the best scores are highlighted in **bold**, while the second-best scores are underlined.

5.1 Image Rescaling

We evaluate image rescaling at rescaling factors $s = 2$ and $s = 4$. For both factors, the model is trained on the DIV2K [1] dataset for 500k iterations using the AdamW optimizer [33] with $\beta_1 = 0.9$, $\beta_2 = 0.99$, and zero weight decay. The learning rate is initialized at 2×10^{-4} and reduced by half at iterations 100k, 200k, 300k, 350k, 400k, and 450k. We utilize a batch size of 16 with randomly cropped 160×160 patches and apply standard geometric augmentations, including horizontal flips and rotations. The loss weights in (17) are set to $\lambda_{\text{HR}} = 1.0$, $\lambda_{\text{LR}} = 5 \times 10^{-2}$, and $\lambda_{\text{dist}} = 10^{-5}$. Model performance is reported on the DIV2K validation set and four standard benchmarks: Set5 [8], Set14 [54], BSD100 [35], and Urban100 [25]. Following established protocols [51, 50, 30], we compute PSNR and SSIM metrics on the Y channel of the YCbCr color space to assess HR image reconstruction.

Results. We evaluate LR2Flow against three categories of rescaling approaches: (i) standard SR approaches using fixed Bicubic downscaling [19, 3, 31, 61, 15, 29, 12]; (ii) encoder-decoder frameworks that jointly learn downscaling and upscaling [27, 44]; and (iii) flow-based rescaling models [51, 30, 6].

Quantitative results presented in Table 1 indicate that SR-only pipelines, including advanced Transformer baselines such as SwinIR and HAT, exhibit limited performance due to their reliance on fixed

Table 1: Quantitative comparison of image rescaling performance (PSNR/SSIM) on benchmark datasets.

Scale	Downscaling & Upscaling	Set5		Set14		BSD100		Urban100		DIV2K	
		PSNR	SSIM								
$\times 2$	Bicubic & Bucibic	33.66	0.9299	30.24	0.8688	29.56	0.8431	26.88	0.8403	31.01	0.9393
	Bicubic & SRCNN [19]	36.66	0.9542	32.45	0.9067	31.36	0.8879	29.50	0.8946	-	-
	Bicubic & CARN [3]	37.76	0.9590	33.52	0.9166	32.09	0.8978	31.92	0.9256	-	-
	Bicubic & EDSR [31]	38.20	0.9606	34.02	0.9204	32.37	0.9018	33.10	0.9363	35.12	0.9699
	Bicubic & RCAN [61]	38.27	0.9614	34.12	0.9216	32.41	0.9027	33.34	0.9384	-	-
	Bicubic & SAN [15]	38.31	0.9620	34.07	0.9213	32.42	0.9208	33.10	0.9370	-	-
	Bicubic & SwinIR [29]	38.42	0.9623	34.46	0.9250	32.53	0.9041	33.81	0.9427	-	-
	Bicubic & HAT [12]	38.91	0.9646	35.29	0.9293	32.74	0.9066	35.09	0.9505	-	-
	TAD & TAU [27]	38.46	-	35.52	-	36.68	-	35.03	-	39.01	-
$\times 4$	CAR & EDSR [44]	38.94	0.9658	35.61	0.9404	33.83	0.9262	35.24	0.9572	38.26	0.9599
	IRN [51]	43.99	0.9871	40.79	0.9778	41.32	0.9876	39.92	0.9865	44.32	0.9908
	T-IRN [6]	44.86	0.9883	41.70	0.9809	42.68	0.9913	41.05	0.9899	45.46	0.9932
	HCFflow [30]	45.08	0.9895	42.30	0.9827	42.61	0.9909	41.92	0.9928	45.66	0.9933
	LR2Flow	46.87	0.9932	43.98	0.9880	44.94	0.9948	43.56	0.9951	47.55	0.9958
	Bicubic & Bicubic	28.42	0.8104	26.00	0.7027	25.96	0.6675	23.14	0.6577	26.66	0.8521
	Bicubic & SRCNN [19]	30.48	0.8628	27.50	0.7513	26.90	0.7101	24.52	0.7221	-	-
	Bicubic & CARN [3]	32.13	0.8937	28.60	0.7806	27.58	0.7349	26.07	0.7837	-	-
	Bicubic & EDSR [31]	32.46	0.8968	28.80	0.7760	27.71	0.7420	26.64	0.8033	29.38	0.9032
$\times 8$	Bicubic & RCAN [61]	32.63	0.9002	28.87	0.7889	27.77	0.7436	26.82	0.8087	30.77	0.8460
	Bicubic & SAN [15]	32.64	0.9003	28.92	0.7888	27.78	0.7436	26.79	0.8068	-	-
	Bicubic & SwinIR [29]	32.92	0.9044	29.09	0.7950	27.92	0.7489	27.45	0.8254	-	-
	Bicubic & HAT [12]	33.30	0.9083	29.47	0.8015	28.09	0.7551	28.60	0.8498	-	-
	TAD & TAU [27]	31.81	-	28.63	-	28.51	-	26.63	-	31.16	-
	CAR & EDSR [44]	33.88	0.9174	30.31	0.8382	29.15	0.8001	29.28	0.8711	32.82	0.8837
	IRN [51]	36.19	0.9451	32.67	0.9015	31.64	0.8826	31.41	0.9157	35.07	0.9318
	T-IRN [6]	36.29	0.9452	32.70	0.9003	31.64	0.8837	31.19	0.9132	35.10	0.9328
	HCFflow [30]	36.29	0.9468	33.02	0.9065	31.74	0.8864	31.62	0.9206	35.23	0.9346
	LR2Flow	37.00	0.9493	33.89	0.9121	32.33	0.8901	33.37	0.9352	35.97	0.9383

downscaling kernels. This result underscores the value of task-aware or content-adaptive downscaling. Although encoder-decoder methods that jointly optimize downscaling and upscaling deliver substantial gains, they often suffer from underconstrained feature learning due to insufficient regularization. In contrast, flow-based models leverage invertibility and density estimation to explicitly model high-frequency residuals. This capability reduces information loss and improves reconstruction quality.

Our proposed LR2Flow significantly enhances HR reconstruction, achieving superior PSNR and SSIM scores compared to prior methods. As illustrated in Figure 1, LR2Flow preserves edges and textures more faithfully, effectively reducing blur and distortion. We attribute these performance gains to the enhanced stability provided by the redundant wavelet tight frame.

5.2 Image Compression

Our compression pipeline integrates the $\times 2$ rescaling model with lossy JPEG compression. To exploit the structural similarity between LR representations in rescaling and compression tasks, we initialize the compression model using weights pretrained on $\times 2$ rescaling. We fine-tune the model for 200k iterations using the AdamW optimizer ($\beta_1 = 0.9$, $\beta_2 = 0.99$, weight decay = 0). The learning rate is initialized at 2×10^{-5} and halved at iterations 50k, 100k, 150k, and 175k. Training employs a batch size of 16, using randomly cropped 160×160 patches and standard geometric augmentations. The objective follows (17), with weights set to $\lambda_{\text{HR}} = 1.0$, $\lambda_{\text{LR}} = 5 \times 10^{-2}$, and $\lambda_{\text{dist}} = 10^{-5}$. During training, we uniformly sample the JPEG quality factor (QF) from the set $\{50, 55, \dots, 90\}$. For evaluation, we report PSNR and SSIM metrics on the Y channel of the YCbCr color space for the Set5, Set14, BSD100, Urban100, and DIV2K validation sets, at QF values of $\{30, 50, 70, 80, 90\}$.

Results. We compare LR2Flow against two categories of rescaling-based compression pipelines: (i) disjoint approaches that pair frozen rescaling models [31, 29, 61, 51] with pretrained JPEG artifact removal

Figure 1: Qualitative comparison of $\times 4$ image rescaling results. Representative examples are selected from the Set14, BSD100, and Urban100 datasets.

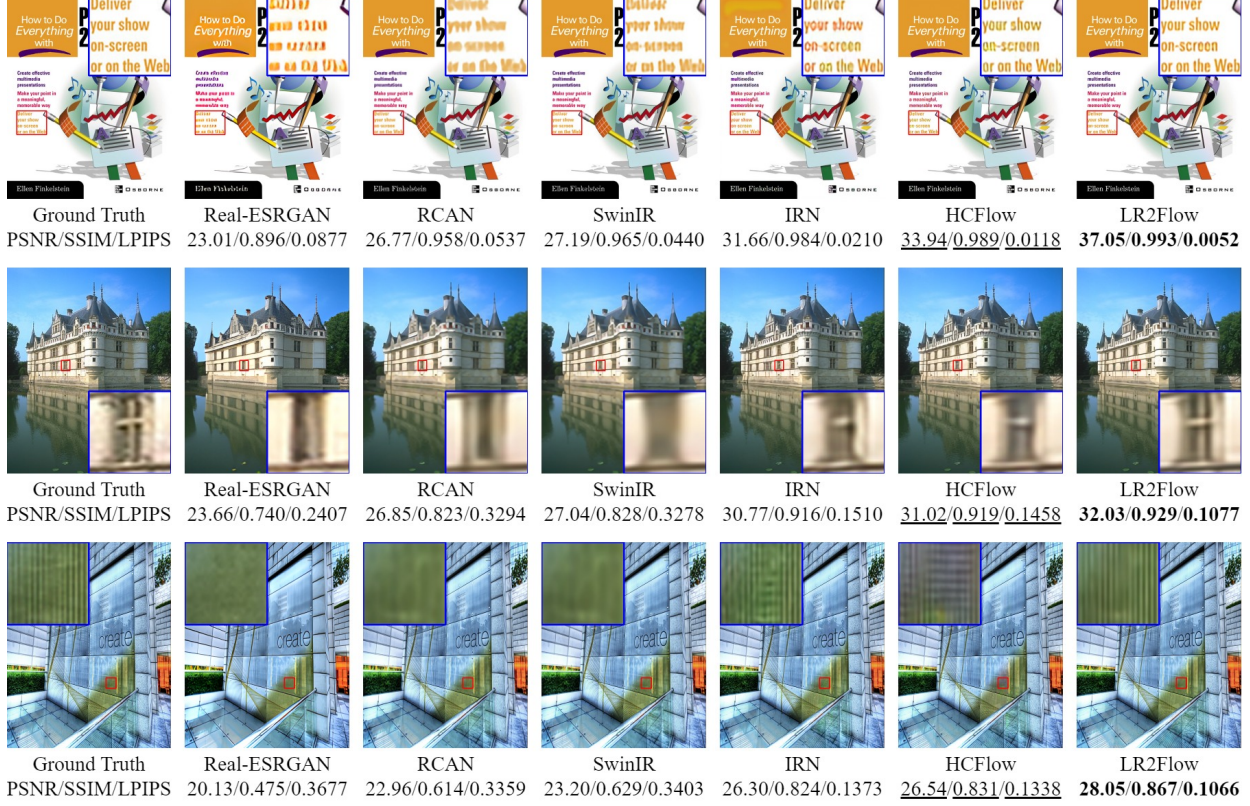


Table 2: Quantitative comparison of rescaling-based compression methods. The rescaling factor is set to $s = 2$.

Downscaling & Upscaling	JPEG QF=30		JPEG QF=50		JPEG QF=70		JPEG QF=80		JPEG QF=90	
	PSNR	SSIM								
Bicubic & Bicubic	30.11	0.8296	30.75	0.8494	31.30	0.8659	31.66	0.8765	32.12	0.8904
Bicubic & EDSR [31]	27.58	0.8166	27.88	0.8352	28.16	0.8512	28.34	0.8616	28.55	0.8755
Bicubic & RCAN [61]	28.57	0.8158	29.00	0.8346	29.34	0.8505	29.56	0.8609	29.85	0.8746
Bicubic & SwinIR [29]	30.65	0.8400	31.56	0.8633	32.45	0.8838	33.11	0.8978	34.17	0.9171
IRN [51]	29.11	0.8133	29.60	0.8334	30.00	0.8509	30.25	0.8621	30.56	0.8767
IRN + CRM [50]	30.41	0.8347	31.61	0.8637	32.13	0.8784	32.76	0.8925	33.67	0.9114
SAIN [53]	<u>31.47</u>	<u>0.8747</u>	<u>33.17</u>	<u>0.9082</u>	<u>34.73</u>	<u>0.9296</u>	<u>35.46</u>	<u>0.9374</u>	<u>35.96</u>	<u>0.9419</u>
LR2Flow	32.37	0.8968	33.98	0.9217	35.15	0.9353	35.71	0.9409	36.12	0.9445

Figure 2: Qualitative comparison of compression results on the DIV2K validation set with a rescaling factor $s = 2$ and JPEG QF=30.

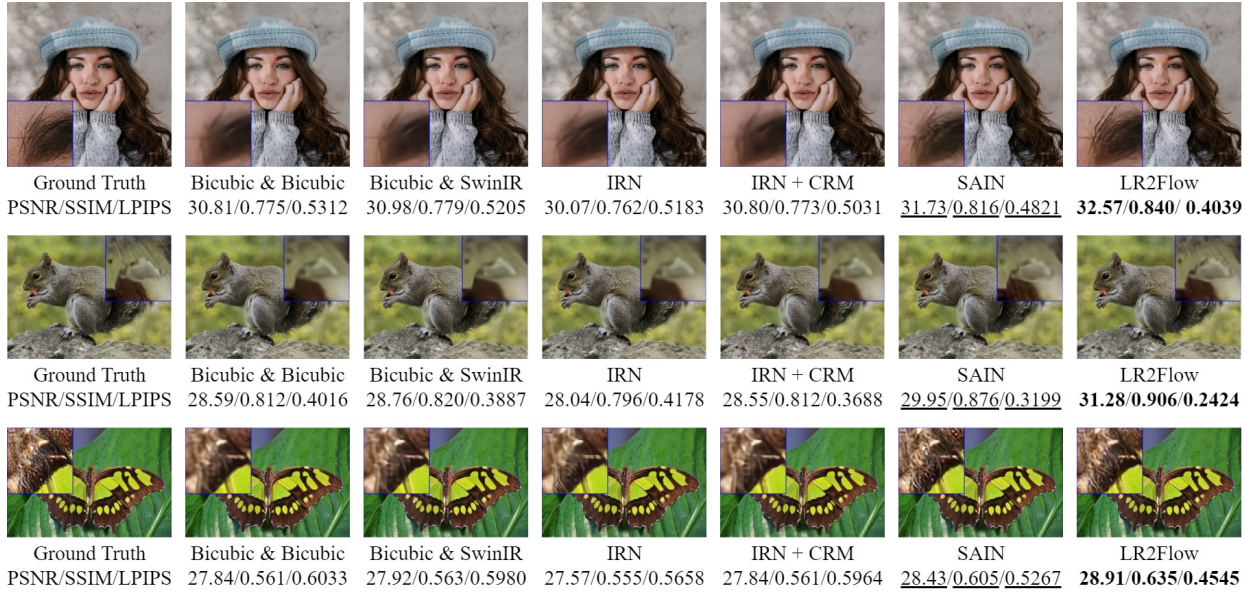
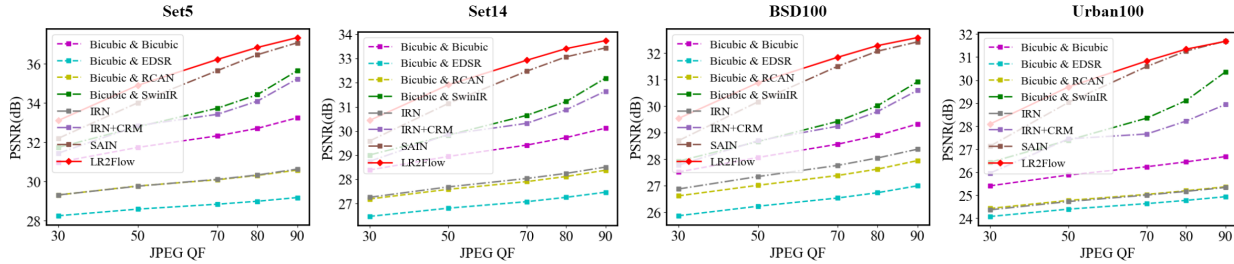


Figure 3: Quantitative comparison of compression performance with $\times 2$ rescaling across various JPEG QFs on the Set5, Set14, BSD100, and Urban100 benchmarks.



networks [26]; and (ii) end-to-end approaches that jointly optimize the rescaling network and the JPEG simulator [53, 50].

Table 2 details the reconstruction performance on the DIV2K validation set. Pipelines utilizing off-the-shelf JPEG decoders with frozen rescaling networks significantly underperform, as fixed upscalers fail to adapt to the specific information loss introduced by lossy compression. While jointly optimizing the rescaling and JPEG decoding narrows this performance gap, such methods typically necessitate auxiliary restoration modules. In contrast, LR2Flow provides a unified framework that learns robust LR representations without requiring auxiliary networks. This design achieves superior performance, particularly at low QFs. Figure 2 presents a qualitative comparison. Disjoint methods suffer from characteristic blocking and ringing artifacts, whereas competing joint optimization methods tend to over-smooth textures. In contrast, LR2Flow effectively mitigates these artifacts while preserving sharp edges, demonstrating its superior capability in modeling high-frequency details. Furthermore, Figure 3 corroborates these gains across all datasets and QF levels, underscoring its robustness and adaptability.

We further evaluate LR2Flow on the rate-distortion (R-D) trade-off, comparing it against standard JPEG and two leading rescaling-based compression methods: IRN+CRM [50] and SAIN [53]. Compression efficiency is measured in bits per pixel (bpp). As shown in Figure 4, LR2Flow exhibits competitive overall

Figure 4: Quantitative evaluation of the R-D trade-off. We report the curves of bpp versus PSNR, SSIM, and LPIPS for the compared compression methods.

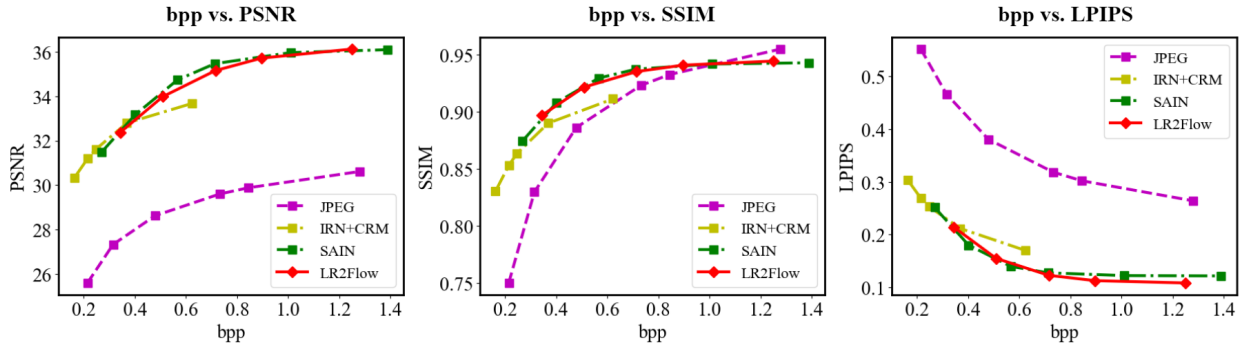


Table 3: Quantitative evaluation of denoising performance (PSNR) for various methods on the CBSD68, Kodak24, McMaster, and Urban100 datasets.

Method	CBSD68			Kodak24			McMaster			Urban100		
	$\sigma_n=15$	$\sigma_n=25$	$\sigma_n=50$									
IRCNN [58]	33.86	31.16	27.86	34.69	32.18	28.93	34.58	32.18	28.91	33.78	31.20	27.70
FFDNet [59]	33.87	31.21	27.96	34.63	32.13	28.98	34.66	32.35	29.18	33.83	31.40	28.05
DnCNN [57]	33.90	31.24	27.95	34.60	32.14	28.95	33.45	31.52	28.62	32.98	30.81	27.59
DSNet [36]	33.91	31.28	28.05	34.63	32.16	29.05	34.67	32.40	29.28	-	-	-
DRUNet [56]	34.30	31.69	28.51	35.31	32.89	29.86	35.40	33.14	30.08	34.81	32.60	29.61
LR2Flow	34.32	31.70	28.50	35.35	32.92	29.88	35.40	33.15	30.08	34.86	32.66	29.65
RPCNN [49]	-	31.24	28.06	-	32.34	29.25	-	32.33	29.33	-	31.81	28.62
BRDNet [46]	34.10	31.43	28.16	34.88	32.41	29.22	35.08	32.75	29.52	34.42	31.99	28.56
RNAN [62]	-	-	28.27	-	-	29.58	-	-	29.72	-	-	29.08
RDN [63]	-	-	28.31	-	-	29.66	-	-	-	-	-	29.38

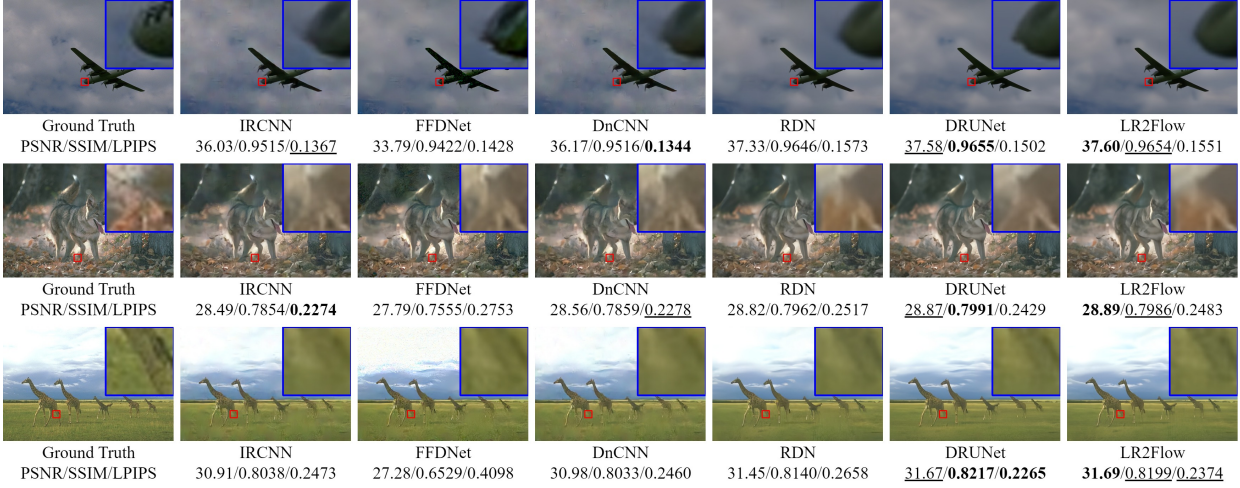
performance and is particularly strong on perceptual metrics, despite not utilizing the auxiliary JPEG-aware decoders employed by IRN+CRM and SAIN. These results validate LR2Flow as a promising approach for high-ratio image compression. It is worth noting that LR2Flow was fine-tuned using (17), which prioritizes reconstruction fidelity while neglecting the entropy of the LR codes. To further improve the R-D curve, a feasible strategy would be to incorporate an explicit rate-distortion regularizer [4, 5] to penalize bit consumption. We leave this direction for future work.

5.3 Image Denoising

We evaluate our denoising approach on the standard additive white Gaussian noise (AWGN) removal task. We train our model for 1M iterations on a composite dataset comprising DIV2K, Flickr2K [31], and the Waterloo Exploration Database [34]. Optimization is performed using AdamW ($\beta_1 = 0.9, \beta_2 = 0.99$, zero weight decay) with an initial learning rate of 2×10^{-4} that is halved every 100k iterations. We use a batch size of 16 with randomly cropped 128×128 patches and apply geometric augmentations. The loss weights in (18) are set to $\lambda_{\text{img}} = 1.0, \lambda_f = \lambda_{\text{hf}} = 10^{-2}$. Training pairs are synthesized by adding AWGN with noise levels σ_n sampled uniformly from the interval [5, 55]. For evaluation, we report PSNR on CBSD68 [35], Kodak24 [23], McMaster [60], and Urban100 at $\sigma_n \in \{15, 25, 50\}$, employing a geometric self-ensemble strategy [47] during inference.

Results. We evaluate the denoising performance of LR2Flow against advanced CNN baselines under two training regimes: (i) unified models trained to handle multiple noise levels [58, 59, 57, 36, 56]; and (ii) noise-specific models trained independently for each noise level [49, 46, 62, 63]. Quantitative results are detailed in Table 3, where LR2Flow demonstrates a distinct advantage over competing methods. Figure 5 further provides visual comparisons at a noise level of $\sigma_n = 50$. While standard CNNs are prone to over-

Figure 5: Qualitative comparison of denoising results on the CBSD68 benchmark at noise level $\sigma_n = 50$.



smoothing and generating hallucinated artifacts under high noise conditions, LR2Flow preserves faithful colors and sharp textures, demonstrating robust detail recovery.

Furthermore, we compare our method against classical model-based baselines, specifically ISTA [16] and TV denoising [40], to evaluate the advantages of LR2Flow’s data-adaptive nonlinear mappings over fixed thresholding strategies. Quantitative comparisons are presented in Table 4. ISTA and TV exhibit a marked performance gap relative to LR2Flow, which underscores the superiority of LR2Flow’s data-adaptive design compared to hand-crafted priors.

Table 4: Quantitative comparison of LR2Flow with classical denoising methods utilizing hand-crafted priors in the image or wavelet domain.

Method	CBSD68			Kodak24			McMaster			Urban100		
	$\sigma_n=15$	$\sigma_n=25$	$\sigma_n=50$									
Total Variation	17.79	17.49	17.08	17.81	17.61	17.33	13.71	13.60	13.42	17.60	17.04	16.25
PixelUnshuffle	24.84	20.54	15.03	25.15	20.96	15.53	25.15	20.96	15.53	24.90	20.64	15.13
ISTA	27.58	24.22	19.59	28.02	24.56	19.68	28.38	25.00	20.22	27.05	23.51	18.98
Haar												
Tight Frame	29.38	26.57	22.80	30.02	27.11	23.04	30.87	27.99	23.83	28.58	25.47	21.65
LR2Flow	34.32	31.70	28.50	35.35	32.92	29.88	35.40	33.15	30.08	34.86	32.66	29.65

5.4 Ablation Study

In this section, we conduct ablation studies to assess the influence of the following factors on model performance: (i) the selection of the wavelet transformation; (ii) the choice of the invertible backbone; and (iii) the trade-off between model size and reconstruction quality.

Comparison of W selection. We evaluate the influence of different choices for the transformation W , specifically comparing the Haar wavelet, the wavelet tight frame, and PixelUnshuffle [42]. Table 5 reports the $\times 2$ rescaling performance using $M = 1$ flow block per level, employing the affine coupling layer (5) as $g_i^{(l)}$. The wavelet tight frame outperforms other configurations by achieving the lowest reconstruction error, validating its theoretical advantage according to Proposition 1. These findings are further corroborated by the results in Table 6, which confirm the superiority of wavelet tight frame across various tasks and invertible architectures.

Comparison of invertible backbones. In Table 6, we compare the performance of the affine coupling layer (5) against the iResBlock (6) when employed as the nonlinear invertible transformation $g_i^{(l)}$ for the $\times 2$ rescaling task. We observe that the affine coupling layer consistently yields superior performance, regardless of the chosen wavelet transformation.

Table 5: Ablation study of \mathbf{W} selection on $\times 2$ rescaling task, configured with $M = 1$ flow block in each flow.

\mathbf{W}	Set5		Set14		BSD100		Urban100	
	PSNR	SSIM	PSNR	SSIM	PSNR	SSIM	PSNR	SSIM
PixelUnshuffle	19.44	0.8163	18.44	0.8132	21.40	0.9057	19.33	0.8720
Haar	35.27	0.9417	31.06	0.8890	30.33	0.8823	29.94	0.9235
Tight Frame	35.55	0.9437	31.30	0.8910	30.62	0.8869	29.75	0.9203

Table 6: Ablation study of the transformation \mathbf{W} and invertible architectures. Experiments are conducted with configurations $T = 1$ and $M = 8$. Results are reported on the DIV2K validation set across three tasks: $\times 2$ image rescaling, image compression ($\times 2$ rescaling with JPEG QF = 30), and image denoising (AWGN with $\sigma_n = 25$).

\mathbf{W}	Rescaling				Compression		Denoising	
	Affine Coupling		iResBlock		PSNR	SSIM	PSNR	SSIM
	PSNR	SSIM	PSNR	SSIM	PSNR	SSIM	PSNR	SSIM
PixelUnshuffle	42.34	0.9863	42.42	0.9869	31.88	0.8937	32.34	0.8918
Haar	45.64	0.9933	41.63	0.9850	31.68	0.8837	32.63	0.8969
Tight Frame	47.55	0.9958	43.19	0.9880	32.37	0.8968	32.84	0.8997

Performance-complexity trade-off. We analyze the scalability of LR2Flow by comparing our standard model and a higher-capacity variant (LR2Flow-L) against an enlarged state-of-the-art baseline (HCFlow-L) on image rescaling tasks. The results in Table 7 indicate that the standard LR2Flow surpasses HCFlow-L, despite having significantly fewer parameters. Moreover, the performance of LR2Flow improves further with increased capacity, highlighting the parameter efficiency and scalability of our approach.

6 Conclusion

We presented LR2Flow, a framework for low-resolution image representation that integrates a wavelet tight frame with normalizing flows. Our theoretical analysis elucidated how the data adaptivity of the wavelet tight frame influences reconstruction performance, particularly given the limited expressivity inherent in invertible architectures. Experimental results validate our analysis. Across image rescaling, compression, and denoising tasks, LR2Flow consistently outperforms comparable methods, demonstrating the effectiveness of our architectural design.

Table 7: Image rescaling results on the DIV2K validation set for different sizes of HCFlow [30] and LR2Flow.

Scale	Model	Params	Set5		Set14		BSD100		Urban100		DIV2K	
			PSNR	SSIM								
$\times 2$	HCFlow	2.07M	45.08	0.9895	42.30	0.9827	42.61	0.9909	41.92	0.9928	45.66	0.9933
	HCFlow-L	4.48M	45.33	0.9893	42.50	0.9828	43.05	0.9918	42.28	0.9933	46.01	0.9939
	LR2Flow	2.74M	46.87	0.9932	43.98	0.9880	44.94	0.9948	43.56	0.9951	47.55	0.9958
	LR2Flow-L	4.95M	47.07	0.9933	44.27	0.9883	45.29	0.9952	44.05	0.9954	47.82	0.9961
$\times 4$	HCFlow	4.35M	36.29	0.9468	33.02	0.9065	31.74	0.8864	31.62	0.9206	35.23	0.9346
	HCFlow-L	9.38M	36.54	0.9483	33.43	0.9115	31.97	0.8899	32.62	0.9307	35.61	0.9379
	LR2Flow	7.15M	37.00	0.9493	33.89	0.9121	32.33	0.8901	33.37	0.9352	35.97	0.9383
	LR2Flow-L	9.36M	37.06	0.9494	33.91	0.9122	32.40	0.8908	33.50	0.9362	36.04	0.9387

A Proofs of Proposition 1, Proposition 2, and (14)

Proof of Proposition 1. When Θ is defined as in (10), the objective function in (9) can be written as

$$J(\rho, \eta) = \mathbb{E}_{q(\mathbf{x})p(\mathbf{z})} \left\| \mathbf{W}_H^\top ((\mathbf{z} - \eta(\mathbf{W}_L \mathbf{x})) \oslash \rho(\mathbf{W}_L \mathbf{x}) - \mathbf{W}_H \mathbf{z}) \right\|^2,$$

where \oslash denote the element-wise division. Fix $\mathbf{x}_L = \mathbf{W}_L \mathbf{x}$ and $\mathbf{x}_H = \mathbf{W}_H \mathbf{x}$, and let $\boldsymbol{\rho} = \rho(\mathbf{x}_L)$ and $\boldsymbol{\eta} = \eta(\mathbf{x}_L)$ for brevity. Note that the i -th element of the vector $\mathbf{W}_H^\top ((\mathbf{z} - \boldsymbol{\eta}) \oslash \boldsymbol{\rho} - \mathbf{x}_H)$ follows a Gaussian distribution with

$$\text{mean} = -\sum_{j=1}^{N-d} [\mathbf{W}_H^\top]_{ij} (\boldsymbol{\eta}_j / \boldsymbol{\rho}_j + [\mathbf{x}_H]_j), \quad \text{variance} = \sigma^2 \sum_{j=1}^{N-d} ([\mathbf{W}_H^\top]_{ij} / \boldsymbol{\rho}_j)^2.$$

Let $q^c = \mathbf{W}_\# q$ denote the distribution of the wavelet coefficients, and let $q_L^c = [\mathbf{W}_L]_\# q$ denote the distribution of the low-frequency coefficients. Then,

$$\begin{aligned} J(\rho, \eta) &= \mathbb{E}_{q^c(\mathbf{x}_L, \mathbf{x}_H)} \left[\sum_{i=1}^d \left| \sum_{j=1}^{N-d} [\mathbf{W}_H^\top]_{ij} (\boldsymbol{\eta}_j / \boldsymbol{\rho}_j + [\mathbf{x}_H]_j) \right|^2 + \sigma^2 \sum_{i=1}^d \sum_{j=1}^{N-d} ([\mathbf{W}_H^\top]_{ij} / \boldsymbol{\rho}_j)^2 \right] \\ &\geq \mathbb{E}_{q^c(\mathbf{x}_L, \mathbf{x}_H)} \left\| \mathbf{W}_H^\top (\boldsymbol{\eta} \oslash \boldsymbol{\rho} + \mathbf{x}_H) \right\|^2 \geq \mathbb{E}_{q_L^c(\mathbf{x}_L)} \text{Tr} (\text{Var} [\mathbf{x}_H | \mathbf{x}_L] \mathbf{W}_H \mathbf{W}_H^\top). \end{aligned}$$

The minimum is attained when $\boldsymbol{\eta} \oslash \boldsymbol{\rho} + \mathbb{E}[\mathbf{x}_H | \mathbf{x}_L] = \mathbf{0}$. \square

Proof of Proposition 2. Let $\mathbf{P} = \mathbf{I} - \mathbf{W}_L^\dagger \mathbf{W}_L$. Define $\boldsymbol{\mu}(\mathbf{x}_L) = \mathbb{E}[\mathbf{W}_H \mathbf{x} | \mathbf{W}_L \mathbf{x} = \mathbf{x}_L]$. Consider a specific mapping $\mathcal{F} \in \Theta$ defined in (12) with $h(\mathbf{x}_H; \mathbf{x}_L) := -\mathbf{x}_H + \mathbf{W}_H(\mathbf{W}_L^\dagger \mathbf{x}_L - \mathbf{P} \boldsymbol{\mu}(\mathbf{x}_L))$. The corresponding reconstruction is given by

$$\hat{\mathbf{x}}(\mathbf{x}_L) = \mathbb{E}_{p(\mathbf{z})} [\mathbf{W}_L^\top \mathbf{x}_L + \mathbf{W}_H^\top h^{-1}(\mathbf{z}; \mathbf{x}_L)] = \mathbf{W}_L^\top \mathbf{x}_L + \mathbf{W}_H^\top \mathbf{W}_H(\mathbf{W}_L^\dagger \mathbf{x}_L - \mathbf{P} \boldsymbol{\mu}(\mathbf{x}_L)).$$

This implies $\mathbf{x} - \hat{\mathbf{x}}(\mathbf{W}_L \mathbf{x}) = \mathbf{W}_H^\top \mathbf{W}_H \mathbf{P}(\mathbf{x} - \boldsymbol{\mu}(\mathbf{x}_L))$. Consequently, we obtain the following bound of the reconstruction error \mathbf{e}^* defined in (9)

$$\mathbf{e}^* \leq \mathbb{E}_{q(\mathbf{x})} \left\| \mathbf{W}_H^\top \mathbf{W}_H \mathbf{P}(\mathbf{x} - \boldsymbol{\mu}(\mathbf{W}_L \mathbf{x})) \right\|^2 = \text{Tr} ((\mathbf{W}_H^\top \mathbf{W}_H)^2 \mathbf{P} \boldsymbol{\Sigma} \mathbf{P}). \quad (19)$$

\square

Proof of (14). Let $J(\mathbf{W})$ denote the upper bound given in (19), where $\mathbf{P} = \mathbf{I} - \mathbf{W}_L^\dagger \mathbf{W}_L$. We have $J(\mathbf{W}) \geq \sum_{i=1}^n (\lambda_i^\uparrow(\mathbf{W}_H^\top \mathbf{W}_H))^2 \cdot \lambda_i^\downarrow(\mathbf{P} \boldsymbol{\Sigma} \mathbf{P})$, with equality when $\mathbf{V}_i^\uparrow(\mathbf{W}_H^\top \mathbf{W}_H) = \mathbf{V}_i^\downarrow(\mathbf{P} \boldsymbol{\Sigma} \mathbf{P})$ for $1 \leq i \leq n$. Here $\mathbf{V}_i^\uparrow(\mathbf{A})$ denotes the eigenspace of $\mathbf{A} \in \mathbb{S}^n$ corresponding to the eigenvalue $\lambda_i^\uparrow(\mathbf{A})$. It follows that $\lambda_i^\downarrow(\mathbf{P} \boldsymbol{\Sigma} \mathbf{P}) = 0$ for $n-d+1 \leq i \leq n$ and $\lambda_i^\downarrow(\mathbf{P} \boldsymbol{\Sigma} \mathbf{P}) \geq \lambda_{i+d}^\downarrow(\boldsymbol{\Sigma})$ for $1 \leq i \leq n-d$. Consequently,

$$J(\mathbf{W}) \geq \sum_{i=1}^{n-d} (\lambda_i^\uparrow(\mathbf{W}_H^\top \mathbf{W}_H))^2 \cdot \lambda_{i+d}^\downarrow(\boldsymbol{\Sigma}).$$

Equality is achieved when $\text{Im}(\mathbf{P}) = \bigoplus_{i=1}^{n-d} \mathbf{V}_i^\uparrow(\boldsymbol{\Sigma})$, i.e., $\text{Im}(\mathbf{W}_L^T) = \bigoplus_{i=1}^d \mathbf{V}_i^\downarrow(\boldsymbol{\Sigma})$. \square

B Proof of Proposition 3

We first prove the following lemma.

Lemma 1. *Let $\mathcal{F} \in \text{Diff}(\mathbb{R}^N)$ be a diffeomorphism. We show that*

$$\begin{aligned} &\mathbb{E}_{q(\mathbf{x})p(\mathbf{z})} \left\| \mathbf{W}^\top \mathcal{F}^{-1}([\mathcal{F}(\mathbf{W}\mathbf{x})]_{1:d}, \mathbf{z}) \right\|^2 \\ &\leq \mathcal{C} \cdot \mathbb{E}_{q(\mathbf{x})} \text{Tr} (\text{Var} [\mathcal{F}(\mathbf{W}_H \mathbf{x})]_{(d+1):N} | \mathcal{F}(\mathbf{W}_H \mathbf{x})]_{1:d}), \end{aligned} \quad (20)$$

where $\mathcal{C} = \int_0^1 \mathbb{E}_{p(\mathbf{z})} \left\| \mathbf{W}^\top (D_H \mathcal{F}^{-1})(\boldsymbol{\xi}_L, \boldsymbol{\xi}_H + t(\mathbf{z} - \boldsymbol{\xi}_H)) \right\|^2 dt$. Here, $\boldsymbol{\xi}_L \in \mathbb{R}^d$ and $\boldsymbol{\xi}_H \in \mathbb{R}^{N-d}$ are reference points, and D_H denotes the partial Jacobian with respect to the high-frequency components.

Proof of Lemma 1. Given \mathbf{x} , let $\mathbf{y} = [\mathcal{F}(\mathbf{W}_H \mathbf{x})]_{1:d}$ and $\mathbf{z}^f = [\mathcal{F}(\mathbf{W}_H \mathbf{x})]_{(d+1):N}$ denote the transformed low- and high-frequency components, respectively. Let $\hat{\mathbf{x}} = \mathbb{E}_{p(\mathbf{z})}[\mathbf{W}^\top \mathcal{F}^{-1}(\mathbf{y}, \mathbf{z})]$ be the reconstruction. Then the reconstruction error writes

$$\mathbf{x} - \hat{\mathbf{x}} = \mathbb{E}_{p(\mathbf{z})} \left[\int_0^1 (\mathbf{W}^\top (D_H \mathcal{F}^{-1}) (\mathbf{y}, \mathbf{z} + t(\mathbf{z}^f - \mathbf{z})))^\top (\mathbf{z}^f - \mathbf{z}) dt \right].$$

Let $g(t, \mathbf{z}) = \mathbf{W}^\top (D_H \mathcal{F}^{-1})(\mathbf{y}, \mathbf{z} + t(\mathbf{z}^f - \mathbf{z}))$. Furthermore, denote $q^f = (\mathcal{F} \circ \mathbf{W})_\# q$ as the model-induced joint coefficient distribution and $q_Z^f = ([\mathcal{F} \circ \mathbf{W}]_{(d+1):N})_\# q$ as the model-induced latent distribution. We show that

$$\begin{aligned} \mathbb{E}_{q(\mathbf{x})} \|\mathbf{x} - \hat{\mathbf{x}}\|^2 &\leq \mathbb{E}_{q^f(\mathbf{y}, \mathbf{z}^f)} \left\| \mathbb{E}_{p(\mathbf{z})} \int_0^1 g(t, \mathbf{z})^\top (\mathbf{z} - \mathbf{z}^f) dt \right\|^2 \\ &\leq \mathbb{E}_{q^f(\mathbf{y}, \mathbf{z}^f)} \left[(\mathbb{E}_{p(\mathbf{z})} \int_0^1 \|g(t, \mathbf{z})\|^2 dt) \cdot (\mathbb{E}_{p(\mathbf{z})} \|\mathbf{z} - \mathbf{z}^f\|^2) \right] \\ &= \mathcal{C} \cdot \mathbb{E}_{q_Z^f(\mathbf{z}^f)p(\mathbf{z})} \|\mathbf{z}^f - \mathbf{z}\|^2, \end{aligned}$$

where $\mathcal{C} = \int_0^1 \mathbb{E}_{p(\mathbf{z})} \|\mathbf{W}^\top D_H \mathcal{F}^{-1}(\xi_L, \xi_H + t(\mathbf{z} - \xi_H))\|^2 dt$ for some reference points $\xi_L \in \mathbb{R}^d$ and $\xi_H \in \mathbb{R}^{N-d}$. In addition,

$$\mathbb{E}_{q_Z^f(\mathbf{z}^f)p(\mathbf{z})} \|\mathbf{z}^f - \mathbf{z}\|^2 = \mathbb{E}_{q_Z^f(\mathbf{z}^f)} \|\mathbf{z}^f\|^2 + (N-d)\sigma^2 \geq \mathbb{E}[\text{Tr}(\text{Var}[\mathbf{z}^f | \mathbf{y}])],$$

with equality holding when $\mathbb{E}[\mathbf{z}^f | \mathbf{y}] = \mathbf{0}$. \square

Proof of Proposition 3. We focus on the subclass of Θ defined in (6), specifically considering mappings of the form

$$\begin{aligned} \mathcal{F} : (\mathbf{x}_L, \mathbf{x}_H) &\mapsto (\mathbf{x}_L + f(\mathbf{x}_L), \mathbf{x}_H + h(\mathbf{x}_H; \mathbf{x}_L)), \\ f : \mathbb{R}^d &\rightarrow \mathbb{R}^d, \text{Lip}(f) \leq L; h(\cdot; \mathbf{x}_L) : \mathbb{R}^{N-d} &\rightarrow \mathbb{R}^{N-d}, \text{Lip}(h(\cdot; \mathbf{x}_L)) \leq L. \end{aligned} \tag{21}$$

Let $q^c = \mathbf{W}_\# q$ denote the distribution of the wavelet coefficients. According to (20), the reconstruction error in (9) is bounded by

$$\mathbf{e}^* \leq \frac{\inf_{f, h \text{ satisfy (21)}} \mathbb{E}_{q^c(\mathbf{x}_L, \mathbf{x}_H)} [\text{Tr}(\text{Var}[\mathbf{x}_H + h(\mathbf{x}_H; \mathbf{x}_L) | \mathbf{x}_L])]}{(1-L)^2},$$

where we use the following properties: (i) $\text{Lip}(\mathcal{F}^{-1}) \leq (1-L)^{-1}$; and (ii) the σ -algebra generated by \mathbf{x}_L coincides with that generated by $\mathbf{x}_L + f(\mathbf{x}_L)$. Furthermore, for the specific case where $h(\mathbf{x}_H; \mathbf{x}_L) = \rho(\mathbf{x}_L) \odot \mathbf{x}_H + \eta(\mathbf{x}_L)$ with $\text{Lip}(\rho) \leq L$, we show that

$$\begin{aligned} \text{Tr}(\text{Var}[\mathbf{x}_H + h(\mathbf{x}_H; \mathbf{x}_L) | \mathbf{x}_L]) &= \text{Tr}(\text{diag}((\mathbf{1}_d + \rho(\mathbf{x}_L))^2) \text{Var}[\mathbf{x}_H | \mathbf{x}_L]) \\ &\leq \|(\mathbf{1}_d + \rho(\mathbf{x}_L))^2\| \cdot \|\text{Var}[\mathbf{x}_H | \mathbf{x}_L]\|_F, \end{aligned}$$

which yields the bound established in (16). \square

C Reconstruction Error Analysis for Orthogonal Transformation

In this case, the hypothesis space is given by

$$\Theta = O(N) = \{ \mathbf{F} \in \mathbb{R}^{N \times N} \mid \mathbf{F} \mathbf{F}^\top = \mathbf{F}^\top \mathbf{F} = \mathbf{I} \}. \tag{22}$$

By focusing on this set, we aim to investigate the inherent limitations of linear models. We derive the following analytic form for the reconstruction error \mathbf{e}^* defined in (9).

Theorem 1. *Let Θ be defined as in (22). Then the minimal reconstruction error defined as in (9) is given by*

$$\mathbf{e}^* = \sum_{i=d+1}^n \lambda_i^\downarrow(\Sigma) + (n-d)\sigma^2. \tag{23}$$

To proof Theorem 1, we utilize the following lemma.

Lemma 2. *Let $\mathbf{W} \in \mathbb{R}^{N \times n}$ satisfies $\mathbf{W}^\top \mathbf{W} = \mathbf{I}$, and $\mathbf{S} \in \mathbb{S}_{++}^n$. Then, the optimal value of the minimization problem*

$$\min_{\mathbf{A} \in \mathbb{R}^{(N-d) \times N}, \mathbf{A}\mathbf{A}^\top = \mathbf{I}} \text{Tr}((\mathbf{W}^\top \mathbf{A}^\top \mathbf{A} \mathbf{W})^2 \mathbf{S}) + \sigma^2 \text{Tr}(\mathbf{W}^\top \mathbf{A}^\top \mathbf{A} \mathbf{W}) \quad (24)$$

is $\sum_{i=d+1}^n \lambda_i^\downarrow(\mathbf{S}) + (n-d)\sigma^2$.

Proof of Lemma 2. For $\mathbf{A} \in \mathbb{R}^{(N-d) \times N}$ satisfies $\mathbf{A}\mathbf{A}^\top = \mathbf{I}$, let $\mathbf{P} = \mathbf{A}^\top \mathbf{A}$. Let $\mathbf{X} = \mathbf{W} \mathbf{S} \mathbf{W}^\top$ and $\mathbf{Y} = \mathbf{W} \mathbf{W}^\top$. The objective in (24) can be rewritten as

$$J(\mathbf{P}) = \text{Tr}(\mathbf{P} \mathbf{Y} \mathbf{P} \mathbf{X}) + \sigma^2 \text{Tr}(\mathbf{P} \mathbf{Y}).$$

Note that: (i) \mathbf{X} and \mathbf{Y} commute: $\mathbf{X}\mathbf{Y} = \mathbf{Y}\mathbf{X} = \mathbf{X}$, implying they can be simultaneously diagonalized; (ii) $\text{Im}(\mathbf{X}) = \text{Im}(\mathbf{Y}) = \text{Im}(\mathbf{W})$. Consequently, there exists $\mathbf{Q} \in O(N)$ such that $\mathbf{X} = \mathbf{Q} \Lambda_X \mathbf{Q}^\top$ and $\mathbf{Y} = \mathbf{Q} \Lambda_Y \mathbf{Q}^\top$, where

$$\Lambda_X = \text{diag}(\lambda_1^\downarrow(\mathbf{S}), \dots, \lambda_n^\downarrow(\mathbf{S}), \mathbf{0}_{N-n}), \quad \Lambda_Y = \text{diag}(\mathbf{1}_n, \mathbf{0}_{N-n}),$$

where $\mathbf{1}_n \in \mathbb{R}^n$ denotes a vector of all ones, and $\mathbf{0}_{N-d} \in \mathbb{R}^{N-d}$ denotes a vector of all zeros. Let $\mathbf{U} = \mathbf{Q}^\top \mathbf{P} \mathbf{Q}$, the objective then writes $J(\mathbf{P}) = \text{Tr}(\mathbf{U} \Lambda_X \mathbf{U} \Lambda_Y) + \sigma^2 \text{Tr}(\mathbf{U} \Lambda_Y)$. We invoke the following results: (i) [Von Neumann's trace inequality] $\text{Tr}(\mathbf{BC}) \geq \sum_{i=1}^m \lambda_i^\downarrow(\mathbf{B}) \lambda_{m-i}^\downarrow(\mathbf{C})$ for Hermitian matrices $\mathbf{B}, \mathbf{C} \in \mathbb{R}^{m \times m}$; and (ii) [Cauchy Interlacing Theorem] For any column orthogonal $\mathbf{V} \in \mathbb{R}^{m \times k}$ and Hermitian $\mathbf{B} \in \mathbb{R}^{m \times m}$, $\lambda_i^\downarrow(\mathbf{B}) \geq \lambda_i^\downarrow(\mathbf{V}^\top \mathbf{B} \mathbf{V}) \geq \lambda_{i+m-k}^\downarrow(\mathbf{B})$, $i = 1, \dots, k$. Consequently,

$$\begin{aligned} \text{Tr}(\mathbf{U} \Lambda_X \mathbf{U} \Lambda_Y) &\geq \sum_{i=1}^N \lambda_i^\downarrow(\mathbf{U} \Lambda_X \mathbf{U}) \lambda_{N-i}^\downarrow(\Lambda_Y) \geq \sum_{i=1}^n \lambda_i^\downarrow(\mathbf{U} \Lambda_X \mathbf{U}) \geq \sum_{i=d+1}^n \lambda_i^\downarrow(\mathbf{S}), \\ \text{Tr}(\mathbf{U} \Lambda_Y) &\geq \sum_{i=1}^N \lambda_i^\downarrow(\mathbf{U} \mathbf{U}) \lambda_{N-i}^\downarrow(\Lambda_Y) = n-d. \end{aligned}$$

The minimum is achieved when $\mathbf{P} = \mathbf{Q} \mathbf{Q}^\top$. \square

Proof of Theorem 1. Let $\mathbf{F} = (\mathbf{F}_1^\top, \mathbf{F}_2^\top)^\top \in O(N)$, where $\mathbf{F}_1 \in \mathbb{R}^{d \times N}$ and $\mathbf{F}_2 \in \mathbb{R}^{(N-d) \times N}$. The reconstruction of \mathbf{x} is given by

$$\hat{\mathbf{x}} = \mathbf{W}^\top \mathbf{F}^\top ([\mathbf{F}(\mathbf{W}\mathbf{x})]_{1:d}, \mathbf{z}) = \mathbf{W}^\top \mathbf{F}_1^\top \mathbf{F}_1 \mathbf{W} \mathbf{x} + \mathbf{W}^\top \mathbf{F}_2^\top \mathbf{z}.$$

Since $\mathbf{W}^\top (\mathbf{F}_1^\top \mathbf{F}_1 + \mathbf{F}_2^\top \mathbf{F}_2) \mathbf{W} = \mathbf{I}$, the reconstruction error can be written as

$$J(\mathbf{F}) = \text{Tr}((\mathbf{W}^\top \mathbf{F}_2^\top \mathbf{F}_2 \mathbf{W})^2 \Sigma) + \sigma^2 \text{Tr}(\mathbf{W}^\top \mathbf{F}_2^\top \mathbf{F}_2 \mathbf{W}).$$

According to Lemma 2, $\mathbf{e}^* = \sum_{i=d+1}^n \lambda_i^\downarrow(\Sigma) + (n-d)\sigma^2$. \square

As demonstrated in Theorem 1, for the linear hypothesis space defined in (22), the reconstruction error \mathbf{e}^* remains invariant to the choice of \mathbf{W} , as the optimal orthogonal mapping naturally aligns the low-frequency subband with the principal components of the data. Nevertheless, linear mappings possess limited expressivity and fail to approximate the optimal solution to (9) for general data distributions $q(\mathbf{x})$. In the following example, we show that a nonlinear invertible mapping \mathcal{F} yields a strictly lower reconstruction error than the linear bound derived in (23). This observation validates the rationale behind the LR2Flow architecture, which employs affine coupling layers and iResBlocks, which have been proven to serve as universal homeomorphism approximators [45, 55].

Example. Consider a two-dimensional zero-mean Gaussian with $\Sigma = \tau^2 \mathbf{I}$. For a LR representation dimension of $d = 1$, the optimal reconstruction error \mathbf{e}^* in (9) is strictly less than the bound $\lambda_2^\downarrow(\Sigma) = \tau^2$ provided in (23).

Proof. Let $(x, y) \sim \mathcal{N}(0, \tau^2 \mathbf{I})$. Consider the polar coordinate transformation $x = \tau r \cos \theta$ and $y = \tau r \sin \theta$, with $r \geq 0$ and $\theta \in [0, 2\pi)$. The joint density is given by $q(r, \theta) = \frac{r}{2\pi} e^{-\frac{r^2}{2}}$, which implies that r and θ are independent with marginals $p(r) = r e^{-\frac{r^2}{2}}$ and $p(\theta) = \frac{1}{2\pi} \mathbb{I}(0 \leq \theta < 2\pi)$. Consequently,

$$\mathbb{E}[(x - \mathbb{E}[x|\theta])^2 + (y - \mathbb{E}[y|\theta])^2] = \mathbb{E}[\tau^2(r - \mathbb{E}[r])^2 (\cos^2 \theta + \sin^2 \theta)] = \tau^2 \text{Var}[r].$$

Direct calculation yields $\mathbb{E}[r] = \sqrt{\frac{\pi}{2}}$ and $\text{Var}[r] = 2 - \frac{\pi}{2}$. We define the nonlinear invertible map as $\mathcal{F} = f \circ \mathbf{W}^\top$, where $f(x, y) = (\theta(x, y), \tau^{-1} \sqrt{x^2 + y^2})$ and $\theta(x, y)$ denotes the angle. By choosing the latent prior $p(z) = \delta(z - \mathbb{E}[r])$, we obtain

$$\mathbb{E}_{q(\mathbf{x})p(z)} \|\mathbf{x} - \mathbf{W}^\top \mathcal{F}^{-1}([\mathcal{F}(\mathbf{W}\mathbf{x})]_{1:d}, z)\|^2 = (2 - \pi/2)\tau^2.$$

Thus, $\mathbf{e}^* \leq (2 - \frac{\pi}{2})\tau^2 < \tau^2 = \lambda_2^\downarrow(\Sigma)$. \square

References

- [1] Eirikur Agustsson and Radu Timofte. Ntire 2017 challenge on single image super-resolution: Dataset and study. In *Proceedings of the IEEE conference on computer vision and pattern recognition workshops*, pages 126–135, 2017.
- [2] Michal Aharon, Michael Elad, and Alfred Bruckstein. K-svd: An algorithm for designing overcomplete dictionaries for sparse representation. *IEEE Transactions on signal processing*, 54(11):4311–4322, 2006.
- [3] Namhyuk Ahn, Byungkon Kang, and Kyung-Ah Sohn. Fast, accurate, and lightweight super-resolution with cascading residual network. In *Proceedings of the European conference on computer vision (ECCV)*, pages 252–268, 2018.
- [4] Johannes Ballé, Valero Laparra, and Eero P Simoncelli. End-to-end optimized image compression. *arXiv preprint arXiv:1611.01704*, 2016.
- [5] Johannes Ballé, David Minnen, Saurabh Singh, Sung Jin Hwang, and Nick Johnston. Variational image compression with a scale hyperprior. *arXiv preprint arXiv:1802.01436*, 2018.
- [6] Jingwei Bao, Jinhua Hao, Pengcheng Xu, Ming Sun, Chao Zhou, and Shuyuan Zhu. Plug-and-play tri-branch invertible block for image rescaling. In *Proceedings of the AAAI Conference on Artificial Intelligence*, volume 39, pages 1826–1834, April 2025.
- [7] Jens Behrmann, Will Grathwohl, Ricky TQ Chen, David Duvenaud, and Jörn-Henrik Jacobsen. Invertible residual networks. In *International conference on machine learning*, pages 573–582. PMLR, 2019.
- [8] Marco Bevilacqua, Aline Roumy, Christine Guillemot, and Marie Line Alberi-Morel. Low-complexity single-image super-resolution based on nonnegative neighbor embedding. 2012.
- [9] Jian-Feng Cai, Bin Dong, Stanley Osher, and Zuowei Shen. Image restoration: total variation, wavelet frames, and beyond. *Journal of the American Mathematical Society*, 25(4):1033–1089, 2012.
- [10] Jian-Feng Cai, Hui Ji, Zuowei Shen, and Gui-Bo Ye. Data-driven tight frame construction and image denoising. *Applied and Computational Harmonic Analysis*, 37(1):89–105, 2014.
- [11] Jian-Feng Cai, Stanley Osher, and Zuowei Shen. Linearized bregman iterations for frame-based image deblurring. *SIAM Journal on Imaging Sciences*, 2(1):226–252, 2009.
- [12] Xiangyu Chen, Xintao Wang, Jiantao Zhou, Yu Qiao, and Chao Dong. Activating more pixels in image super-resolution transformer. In *Proceedings of the IEEE/CVF conference on computer vision and pattern recognition*, pages 22367–22377, 2023.

- [13] Hyomin Choi and Ivan V Bajić. Scalable image coding for humans and machines. *IEEE Transactions on Image Processing*, 31:2739–2754, 2022.
- [14] Ronald R Coifman and David L Donoho. Translation-invariant de-noising. In *Wavelets and statistics*, pages 125–150. Springer, 1995.
- [15] Tao Dai, Jianrui Cai, Yongbing Zhang, Shu-Tao Xia, and Lei Zhang. Second-order attention network for single image super-resolution. In *Proceedings of the IEEE/CVF conference on computer vision and pattern recognition*, pages 11065–11074, 2019.
- [16] Ingrid Daubechies, Michel Defrise, and Christine De Mol. An iterative thresholding algorithm for linear inverse problems with a sparsity constraint. *Communications on Pure and Applied Mathematics: A Journal Issued by the Courant Institute of Mathematical Sciences*, 57(11):1413–1457, 2004.
- [17] Ingrid Daubechies, Bin Han, Amos Ron, and Zuowei Shen. Framelets: Mra-based constructions of wavelet frames. *Applied and computational harmonic analysis*, 14(1):1–46, 2003.
- [18] Laurent Dinh, Jascha Sohl-Dickstein, and Samy Bengio. Density estimation using real nvp. *arXiv preprint arXiv:1605.08803*, 2016.
- [19] Chao Dong, Chen Change Loy, Kaiming He, and Xiaoou Tang. Image super-resolution using deep convolutional networks. *IEEE transactions on pattern analysis and machine intelligence*, 38(2):295–307, 2015.
- [20] David L Donoho. De-noising by soft-thresholding. *IEEE transactions on information theory*, 41(3):613–627, 2002.
- [21] Michael Elad and Michal Aharon. Image denoising via sparse and redundant representations over learned dictionaries. *IEEE Transactions on Image processing*, 15(12):3736–3745, 2006.
- [22] David J Field. Relations between the statistics of natural images and the response properties of cortical cells. *Journal of the Optical Society of America A*, 4(12):2379–2394, 1987.
- [23] Rich Franzen. Kodak Lossless True Color Image Suite, 1999. Accessed: 2024-05-20.
- [24] Vivek K Goyal, Jelena Kovačević, and Jonathan A Kelner. Quantized frame expansions with erasures. *Applied and Computational Harmonic Analysis*, 10(3):203–233, 2001.
- [25] Jia-Bin Huang, Abhishek Singh, and Narendra Ahuja. Single image super-resolution from transformed self-exemplars. In *Proceedings of the IEEE conference on computer vision and pattern recognition*, pages 5197–5206, 2015.
- [26] Jiaxi Jiang, Kai Zhang, and Radu Timofte. Towards flexible blind jpeg artifacts removal. In *Proceedings of the IEEE/CVF International Conference on Computer Vision*, pages 4997–5006, 2021.
- [27] Heewon Kim, Myungsub Choi, Bee Lim, and Kyoung Mu Lee. Task-aware image downscaling. In *Proceedings of the European conference on computer vision (ECCV)*, pages 399–414, 2018.
- [28] Durk P Kingma and Prafulla Dhariwal. Glow: Generative flow with invertible 1x1 convolutions. *Advances in neural information processing systems*, 31, 2018.
- [29] Jingyun Liang, Jiezhang Cao, Guolei Sun, Kai Zhang, Luc Van Gool, and Radu Timofte. Swinir: Image restoration using swin transformer. In *Proceedings of the IEEE/CVF international conference on computer vision*, pages 1833–1844, 2021.
- [30] Jingyun Liang, Andreas Lugmayr, Kai Zhang, Martin Danelljan, Luc Van Gool, and Radu Timofte. Hierarchical conditional flow: A unified framework for image super-resolution and image rescaling. In *Proceedings of the IEEE/CVF International Conference on Computer Vision*, pages 4076–4085, 2021.

[31] Bee Lim, Sanghyun Son, Heewon Kim, Seungjun Nah, and Kyoung Mu Lee. Enhanced deep residual networks for single image super-resolution. In *Proceedings of the IEEE conference on computer vision and pattern recognition workshops*, pages 136–144, 2017.

[32] Yang Liu, Zhenyue Qin, Saeed Anwar, Pan Ji, Dongwoo Kim, Sabrina Caldwell, and Tom Gedeon. Invertible denoising network: A light solution for real noise removal. In *Proceedings of the IEEE/CVF conference on computer vision and pattern recognition*, pages 13365–13374, 2021.

[33] I Loshchilov. Decoupled weight decay regularization. *arXiv preprint arXiv:1711.05101*, 2017.

[34] Kede Ma, Zhengfang Duanmu, Qingbo Wu, Zhou Wang, Hongwei Yong, Hongliang Li, and Lei Zhang. Waterloo exploration database: New challenges for image quality assessment models. *IEEE Transactions on Image Processing*, 26(2):1004–1016, 2016.

[35] David Martin, Charless Fowlkes, Doron Tal, and Jitendra Malik. A database of human segmented natural images and its application to evaluating segmentation algorithms and measuring ecological statistics. In *Proceedings eighth IEEE international conference on computer vision. ICCV 2001*, volume 2, pages 416–423. IEEE, 2001.

[36] Yali Peng, Lu Zhang, Shigang Liu, Xiaojun Wu, Yu Zhang, and Xili Wang. Dilated residual networks with symmetric skip connection for image denoising. *Neurocomputing*, 345:67–76, 2019.

[37] Yuhui Quan, Hui Ji, and Zuowei Shen. Data-driven multi-scale non-local wavelet frame construction and image recovery. *Journal of Scientific Computing*, 63:307–329, 2015.

[38] Amos Ron and Zuowei Shen. Affine systems inl2 (rd): the analysis of the analysis operator. *Journal of Functional Analysis*, 148(2):408–447, 1997.

[39] Daniel Ruderman and William Bialek. Statistics of natural images: Scaling in the woods. *Advances in neural information processing systems*, 6, 1993.

[40] Leonid I Rudin, Stanley Osher, and Emad Fatemi. Nonlinear total variation based noise removal algorithms. *Physica D: nonlinear phenomena*, 60(1-4):259–268, 1992.

[41] Jiawei Shao and Jun Zhang. Bottlenet++: An end-to-end approach for feature compression in device-edge co-inference systems. In *2020 IEEE International Conference on Communications Workshops (ICC Workshops)*, pages 1–6. IEEE, 2020.

[42] Wenzhe Shi, Jose Caballero, Ferenc Huszár, Johannes Totz, Andrew P Aitken, Rob Bishop, Daniel Rueckert, and Zehan Wang. Real-time single image and video super-resolution using an efficient sub-pixel convolutional neural network. In *Proceedings of the IEEE conference on computer vision and pattern recognition*, pages 1874–1883, 2016.

[43] Richard Shin and Dawn Song. Jpeg-resistant adversarial images. In *NIPS 2017 workshop on machine learning and computer security*, volume 1, page 8, 2017.

[44] Wanjie Sun and Zhenzhong Chen. Learned image downscaling for upscaling using content adaptive resampler. *IEEE Transactions on Image Processing*, 29:4027–4040, 2020.

[45] Takeshi Teshima, Isao Ishikawa, Koichi Tojo, Kenta Oono, Masahiro Ikeda, and Masashi Sugiyama. Coupling-based invertible neural networks are universal diffeomorphism approximators. *Advances in Neural Information Processing Systems*, 33:3362–3373, 2020.

[46] Chunwei Tian, Yong Xu, and Wangmeng Zuo. Image denoising using deep cnn with batch renormalization. *Neural Networks*, 121:461–473, 2020.

[47] Radu Timofte, Rasmus Rothe, and Luc Van Gool. Seven ways to improve example-based single image super resolution. In *Proceedings of the IEEE conference on computer vision and pattern recognition*, pages 1865–1873, 2016.

[48] Ce Wang, Zhenyu Hu, Wanjie Sun, and Zhenzhong Chen. Timestep-aware diffusion model for extreme image rescaling. In *Proceedings of the IEEE/CVF International Conference on Computer Vision*, pages 15594–15603, 2025.

[49] Zhihao Xia and Ayan Chakrabarti. Identifying recurring patterns with deep neural networks for natural image denoising. In *Proceedings of the IEEE/CVF winter conference on applications of computer vision*, pages 2426–2434, 2020.

[50] Mingqing Xiao, Shuxin Zheng, Chang Liu, Zhouchen Lin, and Tie-Yan Liu. Invertible rescaling network and its extensions. *International Journal of Computer Vision*, 131(1):134–159, 2023.

[51] Mingqing Xiao, Shuxin Zheng, Chang Liu, Yaolong Wang, Di He, Guolin Ke, Jiang Bian, Zhouchen Lin, and Tie-Yan Liu. Invertible image rescaling. In *Computer Vision–ECCV 2020: 16th European Conference, Glasgow, UK, August 23–28, 2020, Proceedings, Part I 16*, pages 126–144. Springer, 2020.

[52] Jinbo Xing, Wenbo Hu, Menghan Xia, and Tien-Tsin Wong. Scale-arbitrary invertible image downscaling. *IEEE Transactions on Image Processing*, 2023.

[53] Jinhai Yang, Mengxi Guo, Shijie Zhao, Junlin Li, and Li Zhang. Self-asymmetric invertible network for compression-aware image rescaling. In *Proceedings of the AAAI Conference on Artificial Intelligence*, volume 37, pages 3155–3163, 2023.

[54] Roman Zeyde, Michael Elad, and Matan Protter. On single image scale-up using sparse-representations. In *Curves and Surfaces: 7th International Conference, Avignon, France, June 24–30, 2010, Revised Selected Papers 7*, pages 711–730. Springer, 2012.

[55] Han Zhang, Xi Gao, Jacob Unterman, and Tom Arodz. Approximation capabilities of neural odes and invertible residual networks. In *International Conference on Machine Learning*, pages 11086–11095. PMLR, 2020.

[56] Kai Zhang, Yawei Li, Wangmeng Zuo, Lei Zhang, Luc Van Gool, and Radu Timofte. Plug-and-play image restoration with deep denoiser prior. *IEEE Transactions on Pattern Analysis and Machine Intelligence*, 44(10):6360–6376, 2021.

[57] Kai Zhang, Wangmeng Zuo, Yunjin Chen, Deyu Meng, and Lei Zhang. Beyond a gaussian denoiser: Residual learning of deep cnn for image denoising. *IEEE transactions on image processing*, 26(7):3142–3155, 2017.

[58] Kai Zhang, Wangmeng Zuo, Shuhang Gu, and Lei Zhang. Learning deep cnn denoiser prior for image restoration. In *Proceedings of the IEEE conference on computer vision and pattern recognition*, pages 3929–3938, 2017.

[59] Kai Zhang, Wangmeng Zuo, and Lei Zhang. Ffdnet: Toward a fast and flexible solution for cnn-based image denoising. *IEEE Transactions on Image Processing*, 27(9):4608–4622, 2018.

[60] Lei Zhang, Xiaolin Wu, Antoni Buades, and Xin Li. Color demosaicking by local directional interpolation and nonlocal adaptive thresholding. *Journal of Electronic imaging*, 20(2):023016–023016, 2011.

[61] Yulun Zhang, Kunpeng Li, Kai Li, Lichen Wang, Bineng Zhong, and Yun Fu. Image super-resolution using very deep residual channel attention networks. In *Proceedings of the European conference on computer vision (ECCV)*, pages 286–301, 2018.

[62] Yulun Zhang, Kunpeng Li, Kai Li, Bineng Zhong, and Yun Fu. Residual non-local attention networks for image restoration. *arXiv preprint arXiv:1903.10082*, 2019.

[63] Yulun Zhang, Yapeng Tian, Yu Kong, Bineng Zhong, and Yun Fu. Residual dense network for image restoration. *IEEE transactions on pattern analysis and machine intelligence*, 43(7):2480–2495, 2021.